REVISION 1

Word Count: 12085

Raman analysis of octocoral carbonate ion structural disorder along a natural depth gradient, Kona coast, Hawai‘i

Kyle Conner[1], Shiv Sharma[1], Ryohei Uchiyama[2], Kentaro Tanaka[3], Naoko Murakami-Sugihara[3], Kotaro Shirai[3], Samuel Kahng[1]

1. School of Ocean and Earth Science and Technology, University of Hawai'i at Manoa, Honolulu, Hawaii 96822, U.S.A.

2. Graduate School of Science, Hokkaido University, Kita-10 Nishi-8 Kita-ku, Sapporo 060-0810, Japan

3. Atmosphere and Ocean Research Institute, The University of Tokyo, 5-1-5 Kashiwanoha, Kashiwa-shi, Chiba 277-8564, Japan

Abstract

Both environmental and physiological factors cause carbonate ion structural disorder in biogenic Mg-calcites. A major component of this disorder is driven by the incorporation of Mg through environmental forcing and growth rate kinetics although non-Mg factors (e.g., other cation/anion impurities, organic molecules) also contribute. Understanding the drivers of Mg content in biogenic calcite and its effects on disorder has implications for octocoral Mg paleo-proxies and the stability and diagenetic alteration of their calcitic skeletons. However, prior studies of biogenic Mg-calcites have often been complicated by sampling inconsistencies over space and time and potential intra-sample Mg variability. This study aims to analyze the relative contributing factors of octocoral Mg-calcite structural disorder along gradients of both depth and

growth rate. Calcitic octocorals (Corallidae and Isididae, N = 28) were collected from 221–823 m depths across a natural gradient in biogeochemical parameters (pH: 7.4–7.9, T: 5–16°C) off the Kona coast of Hawai‘i Island and analyzed using Raman spectroscopy. Samples were collected during the same month, controlling for potential seasonal variability. Raman spectral parameters from the ν_1 peak quantified total carbonate ion structural disorder (full width at half maximum height [FWHM] of ν_1) and Mg content (ν_1 position, Raman shift). The total structural disorder was then partitioned into Mg-driven and non-Mg driven components (residual ν_1 FWHM). The total structural disorder and Mg content decreased significantly with increasing depth, correlating with temperature and carbonate system parameters. The Mg-temperature relationships from this study were also consistent with prior studies. Non-Mg structural disorder did not correlate to any environmental parameters. When measured across an intra-sample gradient of ontogenetic growth rate, total structural disorder, Mg content, and non-Mg structural disorder increased with growth rate for all but one taxon, demonstrating the kinetic effect of growth rate as well as potential taxon-specific physiological effects. These results provide insight into how environmental and growth rate kinetic effects independently affect different components of carbonate ion structural disorder (Mg content and non-Mg factors). These findings also suggest that Raman spectroscopy may be helpful in quantifying solubility within biogenic calcites.

Keywords: Octocorals, magnesian calcite, carbonate ion disorder, Raman spectroscopy, depth gradient, growth rate kinetics

Introduction

Environmental and physiological (i.e., vital effects) factors can influence carbonate ion structural disorder (referred to hereinafter as structural disorder) within biogenic calcium carbonates ($CaCO_3$) through the incorporation of elemental impurities as well as growth rate kinetics and organic molecules involved in biogenic calcification. $CaCO_3$ structural disorder involves the orientation of carbonate ions relative to the *c* (vertical) and *a* (horizontal) unit cell axes (Bischoff et al. 1985). Ideally, carbonate ions are symmetrically aligned with their respective basal planes along the *a* axis, however, deviations from this symmetry occur at varying extents within synthetic and biogenic $CaCO_3$. The incorporation of non-constituent ion impurities (divalent cations with radii differing from Ca) such as Mg, Sr, and Ba results in altered cation-oxygen bond lengths that can rotate carbonate ions out of the basal plane towards the *c* axis (Bischoff et al. 1985; Urmos et al. 1991; Perrin et al. 2016; Farfan et al. 2018, 2021). Large anions like sulfate (relative to carbonate ions) can also be substituted into the $CaCO_3$ crystal structure and increase structural disorder (reviewed in Vielzeuf et al. 2018). Kinetic effects influenced by growth rate as well as ambient temperature and pressure also promote increased disorder because rapid crystallization reduces the symmetric alignment of carbonate ions and increases the incorporation of impurities (Watson 2004; Morse et al. 2007; Mavromatis et al. 2013; Farfan et al. 2018, 2021). $CaCO_3$ precipitation rates can be elevated through favorable physicochemical conditions obtained either through the exterior environment or within an organism's extracellular calcifying fluid (Al-Horani et al. 2003; Morse et al. 2006; McCulloch et al. 2012). Organic molecules like skeletal organic matrices are crucial in regulating biogenic crystal nucleation and can also introduce disorder by interacting with adjacent carbonate ions as well as other crystallographic features (Tambutté et al. 2011; Mass et al. 2013; DeCarlo et al. 2018; Coronado et al. 2019). Biogenic $CaCO_3$ are known to contain larger unit cell volumes and

69 *c*/*a* axis ratios relative to synthetic $CaCO_3$ even with comparable concentrations of elemental
70 impurities such as Mg (Bischoff et al. 1985). However, it should be noted that Farfan et al.
71 (2021) observed similar unit cell volumes between biogenic (scleractinian coral) and synthetic
72 aragonites.
73 A major component of structural disorder within biogenic calcite (a polymorph of
74 $CaCO_3$) involves the incorporation of Mg cations, which is largely driven by temperature,
75 carbonate system parameters, and skeletal growth rate. Although the exact mechanisms
76 influencing biogenic Mg incorporation are not well understood (Long et al. 2014), the
77 connection between temperature and Mg content in organisms such as octocorals has been well
78 established (Weinbauer et al. 2000; Thresher et al. 2004, 2010; Sherwood et al. 2005). Carbonate
79 system parameters such as saturation state (Ω) have also been correlated with Mg content
80 (Thresher et al. 2011) due to their thermodynamic and kinetic influence on calcite solubility
81 (Mackenzie et al. 1983; Mucci 1987; Morse et al. 2007). Other studies have also highlighted the
82 complications of skeletal growth rate effects on Mg content for calcite (Vielzeuf et al. 2013,
83 2018; Robinson et al. 2014; Chaabane et al. 2019; Flöter et al. 2019) as well as aragonite
84 (Gagnon et al. 2007; Rollion-Bard and Blamart 2015; Bell et al. 2017). The main factor
85 controlling Mg incorporation is still debated, although a combination of different environmental
86 factors (e.g., temperature) simultaneously influencing biological response and growth rate
87 kinetics is generally thought to be the case (Vielzeuf et al. 2018).
88 Understanding the drivers of octocoral Mg content and resulting structural disorder has
89 implications for mineral solubility and Mg paleo-proxies, yet prior studies have been
90 complicated by inconsistencies in sampling location and timeframes as well as potential Mg
91 variability within individual organisms. Higher calcite Mg content generates structural disorder

92 that decreases mineral stability and increases solubility across natural gradients in depth and
93 latitude (Andersson et al. 2008; Lebrato et al. 2016). Mg-temperature relationships are integral to
94 paleothermometry applications, yet the impact of vital effects on Mg incorporation and resulting
95 structural disorder confounds temperature reconstructions (Chaabane et al. 2019). Prior
96 geochemical studies on octocorals relied on limited or opportunistic sample sets lacking in
97 corresponding environmental data with specimens collected from a wide variety of locations and
98 timeframes (Robinson et al. 2014). As a result, attempts to distinguish Mg contributions from
99 different environmental and vital effects are fundamentally confounded. Specimens from
100 different oceanographic regimes contain a different combination of biogeochemical conditions
101 and food sources, which could impact the elemental geochemistry of octocoral skeletons
102 (Hasegawa et al. 2012). Not accounting for time-based variables such as seasonal growth rates
103 could also lead to inaccuracies if samples are collected at different times of the year. Spatial
104 variability in trace elements within individual octocoral skeletons has been analyzed through
105 radial cross section measurements for numerous species, revealing areas of relatively faster
106 growth (e.g., medullar zone for *Corallium rubrum*, Vielzeuf et al. 2008). However, intra-sample
107 variability has not been quantified on surface skeletons despite providing an opportunity to
108 observe the effects of variable growth rates (branches vs. base; Vielzeuf et al. 2008) for skeletons
109 precipitated concurrently under the same environmental conditions. Only a few studies have
110 analyzed octocoral geochemistry with respect to environmental gradients involving
111 corresponding oceanographic parameters (Thresher et al. 2011; Bostock et al. 2015), which have
112 better enabled the analysis of major environmental effects on measured Mg.
113 Raman spectroscopy can provide a fast, nondestructive method of quantifying octocoral
114 structural disorder from Mg and non-Mg sources as well as Mg content. The Raman spectra of

calcium carbonates contain six main peaks: two representing the intermolecular lattice vibration modes (librational L peak and translational T peak) and four representing the internal vibration modes (ν_1, $2\nu_2$, ν_3, ν_4) (Bischoff et al. 1985, [1]Fig. S1). The incorporation of smaller sized (relative to Ca) Mg cations into calcite shortens cation-oxygen bonds, which then elevate the vibrational frequencies and positional disorder of neighboring carbonate ions (Krishnamurti 1957; White 1974; Bischoff et al. 1985). Raman spectral parameters like peak position (Raman shift, cm^{-1}) and width (full width at half magnitude, FWHM, cm^{-1}) increase predictably as a function of Mg content (mol%, Bischoff et al. 1985; Perrin et al. 2016). Incorporated divalent cations larger than Ca such as Ba and Sr generate longer, weaker bonds with oxygen that should, in theory, oppose and suppress the Raman signal influenced by Mg. Analogous work on aragonite minerals reported that ν_1 Raman shift values decrease 0.0544 cm^{-1} per mmol/mol Sr/Ca and 0.0004 cm^{-1} per μmol/mol B/Ca while increasing 0.0262 cm^{-1} per mmol/mol Mg/Ca (Farfan et al. 2021). However, findings from Kaabar et al. (2011) demonstrated that considerable Ba and Sr content (up to 33% of total cations) did not cause significant changes to calcite ν_1 peak Raman shift when the Ca fraction was 20% or higher. Previous Raman calibration of calcite Sr content also observed no significant change in calcite ν_1 peak characteristics even across a 0–13% range in Sr content (Shibano et al. 2017). Sulfate anions thought to impact structural disorder did not significantly change ν_1 Raman shift in calcites with up to 20% $CaSO_4$ (Kontoyannis et al. 1997). While large fractions of Ba, Sr, and S can interact with Ca to significantly alter calcite FWHM values (Kontoyannis et al. 1997; Kaabar et al. 2011), Ba, Sr, and S content within octocoral calcite is negligible based on previous studies (Thresher et al. 2007; LaVigne et al. 2011; Sinclair et al. 2011; Vielzeuf et al. 2018, see [1]Supplementary Info., Figures, and Tables). Observed Raman spectral changes from octocoral calcite can therefore be predominantly attributed to Mg.

The FWHM of biogenic calcite is consistently larger than that of synthetic calcites even at very similar Mg content (Bischoff et al. 1985), suggesting that physiological factors aside from Mg are contributing to overall disorder. As such, the overall ν_1 FWHM signal can be partitioned into Mg and non-Mg driven components (e.g., residual ν_1 FWHM, Comeau et al. 2018; DeCarlo et al. 2019). The residual ν_1 FWHM parameter quantifies structural disorder after the effects of Mg incorporation on overall FWHM have been removed and has been employed in studies of Mg-calcite crustose coralline algae as a potential qualitative proxy of calcifying fluid Ω (Comeau et al. 2018; Cornwall et al. 2018, 2020).

The goals of this study are to separate and analyze the relative contributions of structural disorder with respect to environmental gradients and variable growth effects within octocoral colonies to better understand the drivers of disorder within octocoral calcite. Structural disorder (Mg and non-Mg) as well as Mg content were measured within the calcitic surface skeletons of three Corallidae species and one Isididae genus collected along a natural gradient in depth and environmental parameters (temperature, pH, Ω, salinity) off the Kona coast of Hawai‘i Island within the same month. The study area took advantage of the North Pacific’s naturally compressed vertical oceanographic gradients and shallow calcium carbonate saturation horizons (Greenwood 2009). For the depth gradient Raman measurements, structural disorder and Mg content were measured from the basal portion of skeleton using Raman spectroscopy and compared to corresponding *in situ* oceanographic data to determine the effect of environmental factors on structural disorder while controlling for seasonal and ontogenetic growth effects. Intra-sample Raman measurements were conducted on specific octocoral specimens at varying branch diameters to analyze disorder with respect to variable ontogenetic growth rates under fixed environmental conditions.

Materials and Methods

Octocoral collection and oceanographic observations

Deep-sea octocorals of the families Corallidae and Isididae were collected live along a natural depth gradient (221–823 m, nitrate maximum at ~800 m with pH = 7.35 and DIC = 2340 µmol/kg) off the leeward coast of Hawai‘i Island (Fig. 1, Table 1). Sample collections were made using *Pisces IV/V* submersibles as part of the Hawai‘i Undersea Research Laboratory (HURL) cruises in 2011, 2016, and 2017. All Kona coast specimens were collected within the same four-week period (August to September), thereby minimizing the impacts of seasonal growth variations on Mg content and structural disorder (Mavromatis et al. 2013; Vielzeuf et al. 2013, 2018; Flöter et al. 2019). Moreover, the collection of specimens from the same oceanographic regime minimizes differences in food sources (via surface primary productivity and export) and biogeochemical conditions that can inherently confound results. By controlling for spatial (e.g., sampling location and corresponding oceanography) and temporal (e.g., seasonal growth) variables, environmental factors and species-specific effects can be better isolated. An additional sample (M3) collected off Makapu‘u, O‘ahu at 417 m depth was used for the calibration of Raman-based Mg content. All relevant octocoral specimens (N = 28) were taxonomically identified by specialists at the University of Colombia, Bogotá (Luisa Dueñas; Ardila et al. 2012, Dueñas et al. 2014) and the University of Zürich (Bertalan Lendvay; Lendvay et al. 2020). Octocoral species in this sample set include *Pleurocorallium* cf. *secundum*, *Corallium tortuosum*, *Hemicorallium imperiale/laauense* (a single species complex; Dueñas and Lendvay, pers. comm.), and *Acanella* spp. (likely multiple species). Prior to geochemical analysis, organic matter was removed from the skeletons by soaking and rinsing them in a

sodium hypochlorite (bleach) and water mixture and rinsing with fresh water. For a subset of octocoral skeletons to be measured using Raman and LA-ICPMS (see "Calibration of Raman Mg content" and Table 1), cross sections of the basal skeleton were also cut horizontally to the growth axis using a diamond saw (Isomet 1000, Buehler) and then polished using imperial polishing paper (30 μm, 9 μm, 3 μm, and 1 μm; 3M Inc., Maplewood, MN, USA). No additional polishing of the surface skeleton was carried out (see [1]Supplementary Info., Figures, and Tables).

At each sampling site, oceanographic parameters were measured from the surface down to 1000 m to fully characterize water column chemistry. In the sites visited during the 2011 cruise (Ho'okena, Kealakekua, Wai'ahukini), CTD hydrocasts equipped with a Sea-Bird SBE-9, SBE-18 pH probe, and a rosette of 24 Niskin bottles were conducted at 4–5 stations per site along a 2 km transect perpendicular to the shore. Hydrocasts provided continuous measurements of temperature, conductivity (salinity), and pH as well as discrete water samples (N = 89) that were stored in borosilicate glass bottles in a cool dark container until chemical analysis. Additional continuous temperature, salinity, and pH data were measured using SBE-25 CTD and SBE-18 pH probes attached to the submersible during sample collection. At the Kailua-Kona site, temperature loggers (Onset TidbiT v2) were deployed on the seafloor at nine stations from 200–900 m and collected data every 30 minutes for 12 months (Sept 2016 to Aug 2017, [1]Fig. S2). This additional data enabled the quantification of vertical oscillations in isopycnal depths from internal tides, which aided with accurately aligning environmental parameters with octocoral samples (discussed in [1]Supplementary Info., Figures, and Tables).

Discrete seawater samples were analyzed for carbonate system parameters (pH, DIC, TA) in accordance with standard operation procedures described in Dickson et al. (2007) and Riebesell et al. (2010) with appropriate modifications for differences in our analytical equipment.

Dissolved inorganic carbon (DIC) was measured using an APOLLO SciTech DIC analyzer (model AS-C3). Total alkalinity (TA) was measured using an automated open-cell potentiometric titration method described in Dickson et al. (2007). Certified reference materials (CRM) were measured routinely to confirm measurement accuracy. Spectrophotometric measurements of pH were made using an m-cresol purple dye indicator on a temperature-controlled spectrophotometer (Thermo Scientific^{TM} Orion^{TM} AquaMate 7000 Vis Spectrophotometer). Tris standards (Dickson Lab, SIO) were used to verify dye quality and measurement accuracy. Necessary temperature and salinity measurements were conducted using a YSI multiparameter meter (YSI 5563). CO2SYS (Excel; Lewis and Wallace 1998) was used to calculate calcite saturation state (Ω_{Cal}), [CO_3^{2-}], and [HCO_3^-] using K_1 and K_2 dissociation constants from Mehrbach et al. (1973) refit by Dickson and Millero (1987), K_{HSO4} from Dickson (1990), total boron from Uppström (1974), and seawater-scale pH. Potential density (σ_θ) was calculated in MATLAB using the Gibbs-Seawater toolbox (McDougall and Barker 2011).

Raman measurement and analysis of octocoral surface skeleton

Micro-Raman system. The micro-Raman system located in the Raman and Infrared Spectroscopy Laboratory at the Hawai‘i Institute of Geophysics and Planetology (HIGP) was used to conduct Raman measurements in accordance with procedures used in Acosta-Maeda et al. (2013). The instrument is comprised of a Kaiser Micro-Raman Spectrometer with a RAMAN RXN1^{TM} Microprobe (Kaiser Optical Systems Inc.) and a Leica DMLB microscope with a 100x maximum magnification objective, motorized x-y stage, Kaiser HoloSpec spectrometer, and Andor CCD camera. The near-infrared excitation laser uses an external-cavity Invictus diode laser with a maximum power of 66 mW. The laser wavelength was set at 785 nm to reduce

interference from octocoral skeletal organic matter via residual fluorescence (DeCarlo et al. 2017, 2018; Farfan et al. 2021). The system has a spatial resolution of ~1 μm (using the 100x objective) with a Raman spectral lines measurement accuracy of ±0.5 cm^{-1} and a spectral range of 150–3300 cm^{-1}. Cyclohexane Raman spectra (801.3 cm^{-1} peak) were frequently measured to check for instrument drift over time. The micro-Raman objective was properly focused for every measurement taken. GRAMS/AI software (Thermo Fisher Scientific Inc.) was used to curve fit the Raman ν_1 peak with a mixed Gaussian-Lorentzian curve that allowed the extraction of Raman shift and linewidth (peak width) parameters. Calculating the final FWHM required deconvolving the Raman instrument linewidth from the raw measured linewidth. Deconvolutions were done via Raman measurements of Neon lamp light and the equation:

$$\omega_{obs}^2 = \omega_{actual}^2 + \omega_{inst}^2 \quad (1)$$

where ω_{obs} is the observed linewidth of the Raman peak, ω_{inst} is the instrument-based linewidth, and ω_{actual} is the true linewidth (FWHM) from the analyzed sample. Using relevant ν_1 peak equations from Perrin et al. (2016) (see [1]Supplementary Info., Figures, and Tables), octocoral Mg content was predicted from Raman shift measurements. The resulting Mg value was then used to predict the FWHM signal contributed by Mg (Mg-driven structural disorder, Perrin et al. 2016), which was then subtracted from the overall FWHM measurement to obtain the residual FWHM value (non-Mg structural disorder).

Calibration of Raman Mg content. The accuracy of the calculated Mg values based on the ν_1 Raman shift equation from Perrin et al. (2016) was first verified through the pairing of measurements from Raman spectroscopy and Laser Ablation Inductively Coupled Plasma Mass Spectrometry (LA-ICPMS) on polished octocoral basal cross sections. Radial Mg measurements were conducted on a subset of depth gradient octocorals as well as sample M3 from Makapu‘u

(N = 8, Table 1) using an Agilent 7700cs connected with an excimer laser (NWR-193, New Wave Research) at the Atmosphere and Ocean Research Institute, The University of Tokyo. Setup conditions included a 100-μm diameter laser spot, a pulse rate of 10 Hz and pulse energy of 3 mJ, using He as the carrier gas. The signal intensity of ions (^{26}Mg and ^{43}Ca) was calculated by subtracting the background level of trace elements, which had been obtained empirically with the laser output set to 0%. Subsequently, the ratio of trace elements to ^{43}Ca was obtained and compared to the signal intensities of standard reference materials (discussed in [1]Supplementary Info., Figures, and Tables). Observable round craters in the cross-section surface from the 100-μm laser spot were used to align the subsequent Raman measurements. Raman measurements (N = 10 per marker) were taken adjacent to each crater along the transects. Raman ν_1 Mg estimates were compared to LA-ICPMS Mg to generate a trendline between the two data sources to validate the equations from Perrin et al. (2016) and adjust Raman ν_1 Mg content for the octocoral samples.

Octocoral surface skeleton measurements. Raman measurements were taken on the outermost, up current side of the basal portion (>3 mm diameter) of the octocoral skeleton surface to capture the geochemical conditions at the time of sample collection. Octocorals tend to display skewed growth patterns in their basal cross sections due to consistent variations in radial growth rate in different directions (Luan et al. 2013; Vielzeuf et al. 2018). Growth rates are fastest on the up current side of the corals (opposite of the feeding polyps) and produce relatively thicker growth rings (Kahng, pers. obs.). The central portion of the cross sections contains the fast-growing medullar region (Corallidae) or the central axis (Isididae), which is known to have naturally higher Mg content than the surrounding growth rings (Vielzuef et al. 2008; Perrin et al. 2015; Flöter et al. 2019, Fig. 2). All depth gradient Raman measurements (N = 15 per sample: 3

276 five-point transects with ~100 μm spacing) were taken from the up current side of the thicker
277 basal portion of skeleton (as opposed to younger, thinner branches that are likely comprised of
278 mostly medullar skeleton) to reduce potential growth rate bias in structural disorder and Mg
279 measurements across the depth gradient (Fig. 2). Preliminary sample size analysis demonstrated
280 that at least N = 9 Raman measurements per octocoral sample yield a negligible change in
281 standard error values of ν_1 peak parameters ([1]Fig. S3).
282 Intra-sample Raman measurements were also taken across the surface skeleton of several
283 entire octocoral samples (*P.* cf. *secundum* from 273 m; *C. tortuosum* from 280 m; *H.*
284 *imperiale/laauense* from 444 m; *H. imperiale/laauense* from 472 m; *Acanella* spp. from 823m)
285 to investigate intra-sample variability in structural disorder and Mg content with respect to
286 ontogenetic skeletal growth rates. Because the medullar region/central axis grows relatively
287 faster than the outer annular region, it is assumed that surface skeleton grows relatively faster at
288 thinner branches where the medullar region/central axis is exposed at the surface than thicker
289 basal branches containing annular skeleton at the surface (Vielzeuf et al. 2008; Flöter et al.
290 2019). Five-point transects were taken on 20 different locations along the octocoral surface
291 skeleton (N = 100) to provide a wide coverage of thicker (slower-growing) basal regions and
292 thinner (faster-growing) branches. Branch diameter, the distance between the up current and
293 down current sides, was measured using digital calipers (0.01 mm resolution; Neiko Tools, USA)
294 and then compared to corresponding Raman measurements (ν_1 FWHM, ν_1 Raman shift Mg
295 content, residual ν_1 FWHM) to ascertain variability in structural disorder relative to ontogenetic
296 growth rates.
297 Potential Mg and non-Mg disorder patterns along the depth gradient were compared with
298 corresponding oceanographic measurements to illuminate patterns between skeletal

299 geochemistry and environmental conditions. Univariate models were emphasized as temperature
300 and carbonate system parameters were highly collineated. All relevant statistical analyses were
301 conducted using R Studio (version 4.0.5, R Core Team 2021). For this study, significance was
302 defined as $P < 0.05$.
303
304 **Results**
305 **Environmental context**
306 Oceanographic parameters (temperature, salinity, pH, Ω_{Cal}) decrease sharply at around
307 100 m depth, signifying the transition to denser water masses ([1]Fig. S4). Environmental
308 parameters begin to stabilize past 500 m. The calcite saturation horizon ($\Omega_{Cal} = 1$) is almost
309 reached at ~600 m. Collinearity was also observed in the oceanographic data, especially between
310 pH and temperature ([1]Fig. S4). The sampled octocorals displayed a clear depth zonation pattern
311 with *P.* cf. *secundum* and *C. tortuosum* inhabiting the shallowest areas from ~220 m to ~300 m
312 and *H. imperiale*/*laauense* observed in deeper regions from ~400 m to ~580 m. *Acanella* spp.
313 had a wider depth distribution from ~400 m to over 800 m. Depths from 221 m to 823 m
314 experienced temperature and pH values ranging from 16.37 to 4.99 °C and 7.94 to 7.41,
315 respectively. High-resolution temperature and potential density data are discussed further in the
316 [1]Supplementary Info., Figures, and Tables section.
317
318 **LA-ICPMS corrections to ν_1 Raman shift Mg content**
319 Mg content displayed considerable scatter (~2.5 mol% range) around the linear trendline:
320 LA-ICPMS Mg = (1.1116 × ν_1 Raman shift Mg) + 3.0703 ($R^2 = 0.77$, N = 90) (2)

shown in Figure 3a. There was a noticeable grouping of data points corresponding with the two octocoral species sampled (*H. imperiale/laauense* and *P.* cf. *secundum*). Although the LA-ICPMS Mg values closely overlapped between the two species, Raman-derived Mg values showed greater differences close to 2 mol%. The trendline slope did not differ greatly from the 1:1 line between ν_1 Raman shift Mg and LA-ICPMS Mg, although there was an offset in Mg indicated by the y-intercept where ν_1 underpredicted Mg by 3.86 ± 0.74 mol% on average. Henceforth, corrections based on the linear relationship between LA-ICPMS and Raman are applied to the octocoral ν_1 Raman shift Mg data (depth gradient and intra-sample measurements). Raman-based Mg content appeared to increase significantly towards the medullar region of the cross-section as exemplified with the slow growth axis of *P.* cf. *secundum* from 238 m (Dev. Expl. = 0.94, $R^2 = 0.92$), which had a strong relationship with LA-ICPMS Mg data ($R^2 = 0.79$, $P < 0.001$, Fig. 3b, c).

Octocoral basal surface structural disorder and Mg along depth gradient

FWHM, Mg, and residual FWHM. Octocoral ν_1 FWHM ranged from a high of 10.06 ± 0.03 cm^{-1} detected from *P.* cf. *secundum* at 221 m to a low of 9.11 ± 0.04 cm^{-1} from *H. imperiale/laauense* at 574 m. ν_1 FWHM across all octocoral species significantly decreases with increasing potential density (Fig. 4). *H. imperiale*/*laauense* ν_1 FWHM displayed a significant correlation with potential density, while *Acanella* spp. did not appear to display any notable FWHM patterns ([1]Table S1). *P.* cf. *secundum* ν_1 FWHM had an especially strong correlation with potential density although only four samples were collected. Only two samples of *C. tortuosum* were acquired so no species-specific trendline could be generated for any of the

343 Raman parameters. When only Corallidae octocorals are considered, the ν_1 FWHM depth
344 gradient correlation is further strengthened.

345 Octocoral Mg content (from ν_1 Raman shift) along the depth gradient ranged from a high
346 of 11.54 ± 0.04 mol% $MgCO_3$ detected from *C. tortuosum* at 280 m to a low of 8.97 ± 0.09
347 mol% $MgCO_3$ from *H. imperiale/laauense* at 582 m. Mg content also significantly decreases
348 with increasing potential density (Fig. 4). *H. imperiale*/*laauense* Mg displayed a significant yet
349 weaker correlation with potential density compared to ν_1 FWHM, while *Acanella* spp. Mg
350 displayed no significant pattern with potential density. *P.* cf. *secundum* Mg content was more
351 moderately correlated with potential density compared to ν_1 FWHM ([1]Table S2). The Mg depth
352 gradient correlation is again strengthened when only Corallidae octocorals are considered.

353 Residual ν_1 FWHM ranged from 1.73 ± 0.08 cm^{-1} for *Acanella* spp. at 451 m to 1.21 ±
354 0.04 cm^{-1} for *H. imperiale/laauense* at 399 m and did not change significantly with potential
355 density (Fig. 4, [1]Table S3). Moreover, two-way ANOVA tests yielded no significant species-
356 specific correlations between octocoral residual ν_1 FWHM and those oceanographic parameters
357 (best interaction was between Species and Ω_{Cal}; $F_{3,20} = 1.54$, $P = 0.23$).

358

359 **Correlations with environmental data.** ν_1 FWHM was most strongly correlated with
360 $[CO_3^{2-}]$ and Ω_{Cal} (both R = 0.96), although temperature and pH also displayed strong correlations
361 (Fig. 5, [1]Table S1). ν_1 FWHM from *Acanella* spp. displayed no significant correlations with any
362 environmental parameter. *H. imperiale/laauense* ν_1 FWHM was strongly correlated with all
363 environmental parameters except salinity, with the strongest covariance being with TA (R = -
364 0.86). *P.* cf. *secundum* ν_1 FWHM was well correlated with all environmental parameters.

Mg content had similar correlation patterns compared to ν_1 FWHM although R-values were lower overall. [CO_3^{2-}] and Ω_{Cal} (both R = 0.90) maintained the strongest positive correlations with octocoral Mg content (Fig. 6, [1]Table S2). In *Acanella* spp., the Mg content displayed no significant correlations with any environmental parameter. *H. imperiale/laauense* was moderately correlated with all environmental parameters except for salinity. *P.* cf. *secundum* Mg was well correlated with all environmental parameters except for pH (only moderately correlated), but all linear models had no significant p-values due to low sample size.

Residual ν_1 FWHM was weakly correlated with all environmental parameters with the highest correlation occurring with pH (R = 0.34, [1]Table S3).

Intra-sample octocoral structural disorder and Mg

ν_1 FWHM of *P.* cf. *secundum* collected at 273 m consistently increases at smaller branch diameters from 9.70 ± 0.05 cm^{-1} at 5.18 mm to 9.95 ± 0.04 cm^{-1} at 0.95 mm (Fig. 7a, [1]S7a). Mg content is mostly scattered between 11.22 ± 0.04 mol% and 11.63 ± 0.04 mol% with a notable peak of 11.87 ± 0.08 mol% at 1.77 mm (Fig. 7a, [1]S7a). Residual ν_1 FWHM also increases somewhat both at the smallest branch diameters (from 1.27 ± 0.03 cm^{-1} at 5.64 mm to 1.48 ± 0.04 cm^{-1} at 0.95 mm) and at high branch diameters (e.g., 1.43 ± 0.06 cm^{-1} at 10.13 mm). In *C. tortuosum* from 280 m, both ν_1 FWHM (9.76 ± 0.03 cm^{-1} to 9.76 ± 0.03 cm^{-1}) and residual ν_1 FWHM (1.36 ± 0.02 cm^{-1} to 1.59 ± 0.05 cm^{-1}) increase nonlinearly with decreasing branch diameter, while Mg content increases more linearly from 11.37 ± 0.09 mol% at 7.31 mm to 11.75 ± 0.13 mol% at 1.45 mm ([1]Fig. S7b).

Within the *H. imperiale/laauense* specimen collected at 444 m, ν_1 FWHM sharply increases to 9.87 ± 0.03 cm^{-1} at less than 0.5 mm compared to values of around 9.2–9.4 cm^{-1}

388 from larger diameters (Fig. 7b, [1]S7c). Mg content experiences a similar pattern with values
389 increasing to greater than 10.23 ± 0.07 mol% at diameters less than 0.58 mm. Residual ν_1
390 FWHM increases with decreasing branch diameter at a consistent rate from 1.41 ± 0.01 cm^{-1} at
391 3.67 mm to 1.80 ± 0.02 cm^{-1} at 0.39 mm. In *H. imperiale/laauense* from 472 m, ν_1 FWHM (from
392 9.14 ± 0.02 cm^{-1} at 3.98 mm to 9.47 ± 0.04 cm^{-1} at 0.73 mm) and Mg content (9.02 ± 0.07 mol%
393 to 9.56 ± 0.02 mol% at those same diameters) also increase with decreasing branch diameter at a
394 consistent rate ([1]Fig. S7d). Its residual ν_1 FWHM values follow a similar yet more scattered
395 gradual increase from 1.48 ± 0.02 cm^{-1} at 6.82 mm to 1.70 ± 0.04 cm^{-1} at 0.73 mm. The sharp
396 step-like ν_1 FWHM and Mg spikes observed within the *H. imperiale/laauense* specimens contrast
397 with the more linear and scattered changes within *P.* cf. *secundum* and *C. tortuosum*.
398 In *Acanella* spp. 823 m, a similar pattern is observed between branch diameter and Mg
399 content, which rises from 9.25 ± 0.07 mol% at 8.61 mm to 9.88 ± 0.09 mol% at 1.05 mm (Fig.
400 7c, [1]S7e). However, ν_1 FWHM (9.23 ± 0.03 cm^{-1} at 6.76 mm to 9.03 ± 0.05 cm^{-1} at 1.05 mm) and
401 residual ν_1 FWHM (1.55 ± 0.04 cm^{-1} at 6.76 mm to 1.15 ± 0.04 cm^{-1} at 1.05 mm) contain
402 strikingly different patterns with branch diameter compared to ν_1 FWHM and residual ν_1 FWHM
403 from the other octocoral specimens.
404 Species-specific patterns between branch diameter and overall ν_1 FWHM, Mg-based ν_1
405 FWHM, and residual ν_1 FWHM are apparent (Fig. 8, [1]Table S4). Within *P.* cf. *secundum* from
406 273 m, Mg-based ν_1 FWHM is moderately correlated with overall ν_1 FWHM (R = 0.54), while
407 residual ν_1 FWHM and overall ν_1 FWHM are more strongly correlated (R = 0.77). FWHM values
408 from the *H. imperiale/laauense* specimen collected at 444 m were well correlated with both Mg-
409 based (R = 0.82) and residual ν_1 FWHM (R = 0.82). Strong correlations (R = 0.72 and R = 0.79,
410 respectively) are also observed for *H. imperiale/laauense* from 472 m. ν_1 FWHM has a very

411 strong correlation with residual ν_1 FWHM (R = 0.95) and a strong correlation with Mg-based ν_1
412 FWHM (R = 0.82) within *C. tortuosum* from 280 m. ν_1 FWHM values measured from *Acanella*
413 spp. at 823 m are weakly correlated with Mg-based ν_1 FWHM (R = 0.33) but strongly correlated
414 with residual ν_1 FWHM (R = 0.86).
415
416 **Discussion**
417 **Quantifying Mg content from Raman measurements**
418 Raman spectral measurements of octocoral calcite should be largely representative of
419 changes in Mg content as opposed to other incorporated cations and anions (discussed in
420 Introduction). It should be noted that the range in measured Mg content within the octocorals is
421 narrow, equating to a ν_1 Raman shift range of only 1.09 cm^{-1} for the LA-ICPMS corrections, 0.59
422 cm^{-1} for the depth gradient, and 0.65 cm^{-1} for the intra-sample measurements. However,
423 assuming similar elemental ratios between Mg and other ions like Sr, B, and Ba from Vielzeuf et
424 al. (2018), one would expect to see a range of around 1.92 mmol/mol Sr/Ca, 89.64 μmol/mol
425 B/Ca, and 0.012 μmol/mol Ba/Ca for a Mg/Ca range of 97 mmol/mol. Changes in Mg should
426 again dominate the ν_1 Raman signal (e.g., based on Farfan et al. 2021, +2.54 cm^{-1} from Mg with
427 only -0.10 cm^{-1} from Sr), yet the presence of non-Mg cations could lead to underestimated ν_1
428 Raman shift Mg values. For this reason, the LA-ICPMS Mg correction is needed to obtain more
429 accurate Mg values from ν_1 Raman shift. While the results of Farfan et al. (2021) provide a
430 potential detailed look into the effects of certain divalent cations on Raman spectral analysis of
431 $CaCO_3$, a detailed analogous analysis on calcite minerals is needed.
432 The trendline (Eqn. 2) comparing LA-ICPMS and ν_1 Raman shift Mg displays a
433 consistent offset of around 3 mol% from the 1:1 line with Raman shift underestimating LA-

ICPMS Mg (Fig. 3a). The Raman-Mg calibration lines from Perrin et al. (2016) are based on calcites synthesized under high pressure and temperature without the presence non-Mg cations/anions, organic molecules, or other physiological factors that could impact the calcite Raman signal. It is possible that the presence of non-Mg cations/anions in the octocoral skeleton are contributing to the underestimated ν_1 Raman shift Mg values in this case. Raman shift values within biogenic Mg-calcites are also known to be slightly lower than their synthetic counterparts at similar Mg content (Bischoff et al. 1985). The consistent offset of the LA-ICPMS and Raman trendline suggests that these biogenic factors are largely similar across the octocoral species in this study. There is a notable spread of data points around the trendline that could be due to the differing spatial resolutions of LA-ICPMS (100 μm) and Raman (~2 μm). Octocoral skeletons are known to contain fine-scale spatial variability in Mg content (Vielzeuf et al. 2008). While smaller differences in Mg content are being masked by the spatial mismatch between the two methods, larger Mg differences are better resolved. For instance, Figs. 3b-c highlight the sharp increase in Mg content from the skeletal surface to the medullar region within a single cross section sample of *P.* cf. *secundum*, resulting in a strong LA-ICPMS and ν_1 Raman shift Mg trendline with relatively less scatter. Nevertheless, a strong correlation exists between the two methods with a consistent offset, thus allowing ν_1 Raman shift Mg content to be corrected.

Environmental drivers of structural disorder and Mg

Overall ν_1 FWHM and Mg content both decrease across the environmental gradient, indicating an overall decrease in structural disorder correlating strongly with decreasing temperature and carbonate system parameters. The relationship between potential density (depth) and ν_1 FWHM and Mg content agrees with prior findings along environmental gradients

(Andersson et al. 2008; Thresher et al. 2011). Lower temperatures at greater depth result in a thermodynamically more soluble Mg-calcite structure relative to warmer, shallower waters (Mucci 1987; Morse et al. 2007). Conditions less conducive to calcification at depth (reduced pH, $[CO_3^{2-}]$, and Ω_{Cal}) would also lead to thermodynamically less stable calcite, which discourages Mg incorporation (Mackenzie et al. 1983). Although the relationship between calcite Mg content and temperature has received relatively more attention, carbonate system parameters maintain the highest correlations with ν_1 FWHM and Mg in this study with strong temperature correlations as well.

Non-Mg driven structural disorder measured using residual ν_1 FWHM displayed no clear pattern with depth or environmental parameters. Residual ν_1 FWHM decreases slowly with depth only among the shallowest *C. tortuosum* and *P.* cf. *secundum* specimens, yet the variable clustering from deeper *H. imperiale/laauense* and Isididae disrupts any overall trends. The lack of significant change in non-Mg disorder with depth suggests that the octocoral calcite stability influenced by vital effects or growth rate kinetics not involving Mg are not sensitive to environmental changes. In contrast, ν_1 FWHM and Mg display strong patterns with depth, which implies that skeletal structural disorder is due largely to Mg incorporation. If the majority of non-Mg structural disorder is driven by variations in growth rate, then Mg should dominate the ν_1 FWHM signal given that seasonal growth rates are controlled through a consistent sampling protocol over time and location within the sample (basal portion of surface skeleton). Another possibility is that basal skeleton growth rate itself does not change significantly with depth, which has been observed by Thresher et al. (2016) for Isididae.

ν_1 FWHM could also be positively correlated with extracellular calcifying fluid Ω (Ω_{ECF}) due to the well-recognized positive relationship between calcite growth rates and Ω (Morse et al.

2007). For biogenic calcifiers, higher Ω_{ECF} should drive faster skeletal accretion rates, which would increase structural disorder and ν_1 FWHM values. While this relationship has been well demonstrated for aragonite and used to quantify shallow water coral Ω_{ECF} (DeCarlo et al. 2019), it has not yet been verified for Mg-calcite. Prior studies have used residual ν_1 FWHM as a qualitative proxy for Ω_{ECF} within Mg-calcite calcifiers (e.g., crustose coralline algae, Comeau et al. 2018; Cornwall et al. 2018, 2020) assuming that the Mg-calcite FWHM-Ω_{ECF} relationship operates similarly to that of synthetic and coral aragonite (DeCarlo et al. 2017; Farfan et al. 2021). If true, then the results here would indicate that Ω_{ECF} is not sensitive to the environmental gradient. While this result would have interesting implications for octocoral responses to contemporary carbonate chemistry gradients as well as ongoing ocean acidification, a systematic calibration between calcite Ω_{ECF} and Raman spectral parameters (e.g., FWHM) is needed to confirm these results.

Mg-temperature relationships in this study align with relationships from prior studies of synthetic and biogenic calcite (Fig. 9, [1]Table S6). The linear expression for skeletal Mg/Ca as a function of temperature based on all available octocoral samples from this study ($R^2 = 0.70$, N = 28) as well as the one derived exclusively from Corallidae ($R^2 = 0.73$, N = 23) either overlapped or were similar to those established for *Corallium* spp., *C. rubrum*, and *Corallium* spp. compiled in previous studies (Chave 1954; Weinbauer et al. 2000; Yoshimura et al. 2011; Vielzeuf et al. 2013; Thresher et al. 2016; Chaabane et al. 2019). Only the model from Weinbauer et al. (2000) ($R^2 = 0.99$, N = 3) had a very different slope and intercept. Isididae from this study ($R^2 = 0.20$, N = 5) did not display a strong relationship albeit with a low sample size. The Isididae model generated by Thresher et al. (2016) ($R^2 = 0.87$, N = 73) was similar to prior Corallidae models. Inorganic high-Mg calcite experiments under varying temperatures (5–40°C) also yielded a slope

503 overlapping with the above octocoral studies although the intercept was much lower (Mucci
504 1987). The comparable Mg-temperature slopes between organic and inorganic calcite suggest a
505 similar kinetic Mg incorporation mechanism (Thresher et al. 2016). Meanwhile, differences in
506 intercept values among different octocoral Mg models could result from species-specific effects.
507 The lack of a consistent intra-annual Mg-temperature relationship in prior studies is likely driven
508 by interference from vital effects amplifying Mg content (Vielzeuf et al. 2013). Nevertheless,
509 vital effects can be a product of temperature as well as other environmental parameters. While
510 seasonal fluctuations in skeletal growth rate appear to drive intra-annual Mg variability, longer-
511 term mean temperature has been correlated with average octocoral Mg content (Chaabane et al.
512 2019), a result that could be observed here along the depth gradient.
513
514 **Growth rate effects on structural disorder and Mg**
515 Within individual octocoral specimens, the change in residual ν_1 FWHM with respect to
516 branch diameter differs from that of Mg content despite experiencing the same environmental
517 history. Intra-sample Raman measurements can examine structural disorder as a function of
518 changes in skeletal growth rate driven entirely by organismal physiology and not by
519 environmental conditions. Octocoral branches grow lengthwise and radially (branch
520 width/diameter) over time. As branches increase in length, the medullar or central axis skeleton
521 is precipitated first. As the branch thickens via radial growth, the medullar skeleton eventually
522 transitions to an annular skeleton containing observable growth rings (Fig. 2). Because growth
523 rates are relatively higher within the interior medullar zone and central axis of Corallidae and
524 Isididae skeleton, respectively (Vielzeuf et al. 2008; Flöter et al. 2019), radial growth rates of
525 surface skeleton should be faster for smaller branch diameters and relatively slower at larger

ones. This pattern is further implied by the increase in residual ν_1 FWHM (non-Mg disorder) with decreasing branch diameter (Fig. 7). Linear changes in residual ν_1 FWHM with respect to branch diameter, as opposed to stepwise changes observed for Mg discussed later, could be a result of ontogenetic growth effects where radial growth rates naturally and gradually decrease with age and size (Sinclair et al. 2011; Farmer et al. 2015; Flöter et al. 2019). Thicker, older sections of the branch with relatively slower surface skeletal growth rates would have less non-Mg structural disorder compared to thinner, younger branches. The differing residual ν_1 FWHM pattern observed within *Acanella* spp. (Fig. 7c, [1]S7e) is puzzling since greater non-Mg disorder was also expected within the faster growing central axis of Isididae. This inverted pattern is also well manifested in the overall ν_1 FWHM signal despite Mg content increasing with decreasing branch diameter. Further intra-sample analysis of *Acanella* spp. surface skeleton is needed to confirm whether this outcome is simply an anomaly or the result of a consistent taxon-specific mineralogical difference. Ω_{ECF} could also at least partially contribute to these intra-sample patterns although such interpretations must be approached with caution. It should also be noted that ontogenetic skeletal growth rates are not necessarily the same as crystal growth rates which influence structural disorder and Mg incorporation. For instance, crystal growth rates could occur at the same gradual rate as the bulk skeleton or in spontaneous pulses (Vielzeuf et al. 2018). As branch diameter (i.e., skeletal growth rate) varies, correlations between residual ν_1 FWHM and ν_1 FWHM are comparable to that of Mg content and ν_1 FWHM (Fig. 8, [1]Table S4). Non-Mg growth rate kinetics appears to contribute more towards overall intra-sample structural disorder relative to the environmental gradient, where only Mg and ν_1 FWHM were significantly correlated (Fig. 4).

548 Stepwise increases in Mg content with decreasing octocoral branch diameter are
549 indicative of faster-growing medullar or central axis skeleton, which typify ontogenetic growth
550 patterns in Corallidae and Isididae (Vielzeuf et al. 2008; Sinclair et al. 2011). Significant
551 increases in Mg content were observed with decreasing branch diameter, especially at diameters
552 smaller than 2 mm (Fig. 7). This value agrees with spatially mapped Electron Microprobe
553 Analysis (EMPA) data of Corallidae (*C. rubrum*) cross sections where the diameter of the
554 medullar region containing higher Mg was 1.0–2.0 mm with an irregular shape (Vielzeuf et al.
555 2008; Fig. 2, 3b). For Isididae, the central axis is known to be much rounder with a maximum
556 diameter of 1.0 mm (Flöter et al. 2019). The outer edge of the central axis skeleton in *Acanella*
557 spp. was likely detected through the sharp Mg peak at 1.05 mm diameter. As observed with
558 residual ν_1 FWHM, the early growth medullar zone would intuitively be exposed at the branch
559 tip surface, resulting in Mg spikes at the smallest branch diameters. Elevated Mg content in these
560 regions is likely a product of kinetic effects driven by skeletal growth rates (reviewed in Vielzeuf
561 et al. 2018). In scleractinian skeletons, Gagnon et al. (2007) noted that high Mg regions (also
562 known as Centers of Calcification) were influenced by non-Rayleigh processes in contrast to the
563 rest of the skeleton. Mechanisms such as the growth entrapment model (Watson 2004) as well as
564 a more modified impurity incorporation/repulsion model (Vielzeuf et al. 2018) have been
565 proposed to explain the connection behind precipitation rate and Mg incorporation. The presence
566 of differing organic molecules within rapid growth zones is also thought to selectively enhance
567 Mg incorporation (Gagnon et al. 2007). Regardless of the exact mechanism, these differing
568 growth regions demonstrate the need to focus comparative octocoral surface Mg measurements
569 at the thicker basal portions of skeleton to avoid accidental sampling of the medullar zone.
570

571 **Species-specific patterns**

572 Analysis of intra-sample Mg and non-Mg structural disorder reveals potentially different
573 biomineralization patterns among closely related Corallidae species (*H. imperiale/laauense*, *C.*
574 *tortuosum*, *P.* cf. *secundum*; Ardila et al. 2012) as well as Isididae. Throughout most of the intra-
575 sample specimens, Mg-based ν_1 FWHM and residual ν_1 FWHM are both well correlated with
576 overall ν_1 FWHM although the strength of these correlations varies by species. Some species
577 patterns (e.g., *P.* cf. *secundum*) appear to be more strongly influenced by non-Mg sources
578 compared to others (e.g., *H. imperiale/laauense*) (Fig. 8, [1]Table S4). Mg and residual ν_1 FWHM
579 are positively correlated within *C. tortuosum* and *H. imperiale*/*laauense* while being negatively
580 correlated in *P.* cf. *secundum*. The high variability between the two parameters, however,
581 resulted in no significant trends except for *C. tortuosum*. *P.* cf. *secundum* and *C. tortuosum* also
582 displayed relatively lower residual ν_1 FWHM values despite having the highest Mg content. Mg
583 content and residual ν_1 FWHM were expected to be positively correlated since both are
584 positively impacted by skeletal growth rates (DeCarlo et al. 2017; Vielzeuf et al. 2018). This
585 outcome is only seen within *C. tortuosum* where both Mg and non-Mg structural disorder
586 strongly contribute to overall structural disorder pattern. The lower residual ν_1 FWHM values
587 within the *P.* cf. *secundum* and *C. tortuosum* specimens could be evidence of a species-specific
588 biomineralization effect given the concurrent similarity in ν_1 FWHM results between the two *H.*
589 *imperiale/laauense* specimens. Despite this similarity in ν_1 FWHM, *C. tortuosum* is
590 taxonomically more closely related to *H. imperiale/laauense* than *P.* cf. *secundum* (Ardila et al.
591 2012). Another instance of taxon-specific biomineralization is observed with *Acanella* spp.,
592 which displayed unforeseen ν_1 FWHM and residual ν_1 FWHM patterns with branch diameter.
593 Although these results were surprising considering the known radial growth patterns for Isididae

(Flöter et al. 2019), *Acanella* spp. resides in a different taxonomic family compared to the remaining specimens.

LA-ICPMS and ν_1 Raman shift Mg data also display indications of species-specific patterns in octocoral Mg and non-Mg disorder. *H. imperiale/laauense* and *P.* cf. *secundum* cross sections from multiple depths were used in the analysis of LA-ICPMS and ν_1 Raman shift Mg data. Despite an overlap of LA-ICPMS Mg content between the two species (~10.5–11.2 mol%), Mg content based on ν_1 Raman shift forms two distinct species-specific groups (Fig. 3a). Grouping is also observed with corresponding ν_1 FWHM data, although residual ν_1 FWHM does not appear to show any significant patterns ([1]Fig. S8). Like the intra-sample analysis, residual ν_1 FWHM values within *P.* cf. *secundum* are similar to those of *H. imperiale/laauense* despite the former having greater ν_1 FWHM and Mg content than the latter ([1]Fig. S9 and [1]Table S5). Overall structural disorder and vibrational frequencies are greater in *P.* cf. *secundum* compared to *H. imperiale/laauense* even at areas with the same LA-ICPMS Mg content. Increasing calcite unit cell volumes are thought to lead to lower vibrational frequencies (lower Raman shift) and structural disorder (Bischoff et al. 1985). In this case, *H. imperiale/laauense* specimens could have characteristically larger unit cell volumes compared to *P.* cf. *secundum* specimens. As previously mentioned, the general discrepancies between LA-ICPMS and ν_1 Raman shift Mg content could be attributed to physiological mechanisms absent from the synthetic calcites used in Perrin et al. (2016). Both ν_1 Raman shift and ν_1 FWHM-based trendlines are mostly offset from the 1:1 line through the y-intercept, suggesting that physiological factors contributing to the Mg discrepancy could be largely similar across different octocoral individuals and species. However, the slope of the ν_1 FWHM trendline (0.79 ± 0.04) is offset more compared to that of ν_1 Raman shift (1.11 ± 0.06), indicating that different parts of the LA-ICPMS/Raman FWHM

617 signal (e.g., from different species) are being impacted differentially. The Mg-driven disorder
618 appears to be relatively higher for *P.* cf. *secundum* compared to *H. imperiale/laauense*.
619 Skeletal morphologies could also explain observed differences in Mg and non-Mg driven
620 disorder with respect to changes in branch diameter and growth rate. Stepwise increases in Mg
621 content are apparent within *H. imperiale/laauense* and *Acanella* spp. but occur to a lesser extent
622 within *P.* cf. *secundum* and *C. tortuosum* (Fig. 7, [1]S7).For instance, *C. tortuosum* exhibits linear
623 (or close to linear) trendlines for Mg and non-Mg structural disorder with respect to branch
624 diameter, which could be caused by a more gradual change in disorder and Mg content between
625 the medullar and annular zones (as opposed to sharper transitions in *H. imperiale/laauense*).
626 Faster-growing medullar zones may not be well defined for some individual octocorals, thereby
627 resulting in a less obvious change in structural disorder and Mg. While the intra-sample *P.* cf.
628 *secundum* specimen displayed inconsistent Mg patterns, one specimen of *P.* cf. *secundum*
629 analyzed by LA-ICPMS and Raman displayed a sharp radial increase in Mg content (Fig. 3b, c).
630 A possible explanation of this phenomenon could be connected to skeletal morphology rather
631 than inherent species-specific differences in medullar skeleton characteristics. For instance, the
632 robust skeletons of *P.* cf. *secundum* (as well as *C. tortuosum*) quickly transition from thick basal
633 branches to warped irregular branch tips compared to the smoother transitions in *H.*
634 *imperiale/laauense* (Fig. 7, [1]S7). Less consistent Mg patterns with branch diameter could be a
635 product of inconsistencies in the assumed relationship between ontogenetic growth rate and
636 branch diameter caused by the irregular skeletal morphology itself. Based on the patterns
637 observed with *P.* cf. *secundum* and *C. tortuosum*, branch diameter may not be as reliable of a
638 growth rate metric for the irregular morphologies of those species compared to *H.*
639 *imperiale/laauense*. Whether the formation of this differing skeletal morphology significantly

alters any of the mechanisms (e.g., growth kinetics, non-Rayleigh mechanisms, biomolecules) thought to influence structural disorder and Mg content within the medullar zone is unknown (Gagnon et al. 2007; Tambutté et al., 2011).

Implications

ν_1 FWHM, Mg, and calcite mineral stability

Mg measurements alone do not appear to entirely capture the factors impacting biogenic Mg-calcite disorder and therefore stability. Mg has been demonstrated to be a major driver of structural disorder within synthetic and biogenic calcites, although other sources of disorder can originate from non-Mg sources such as organic molecules and other physiological effects from calcification (Bischoff et al. 1985; Perrin et al. 2016). Data from this study has shown instances where octocoral specimens of very similar Mg content differed in their overall ν_1 FWHM, a result likely to occur from additional structural disorder from non-Mg sources (residual ν_1 FWHM). For example, while the intra-sample Mg content from *P.* cf. *secundum* and *C. tortuosum* overlapped heavily, ν_1 FWHM values from the latter often exceeded that of the former (Fig. 7, [1]S7). ν_1 Raman shift Mg and ν_1 FWHM data from the depth gradient samples are well correlated but express a nonlinear pattern indicating that there are factors influencing ν_1 FWHM differently from Mg. The EMPA-based Mg and ν_1 FWHM calibration lines from Perrin et al. (2016) are also nonlinear as opposed to their strongly linear ν_1 Raman shift Mg calibration lines. Intra-sample ν_1 FWHM and Mg correlations also varied strongly among different species, which is likely driven by variable species-specific skeletal growth rates. Clearly, non-Mg structural disorder can impact the overall ν_1 FWHM signal independently from Mg.

662 Raman spectroscopic measurements of calcite ν_1 FWHM could theoretically provide a
663 quantitative proxy for solubility although empirical validations must first be performed. Mg has
664 served as a prominent proxy for synthetic and biogenic calcite solubility through its correlations
665 with carbonate chemistry along depth and latitudinal gradients (Andersson et al. 2008; Lebrato et
666 al. 2016). While Mg-based metrics of solubility are valid for synthetic calcites, biogenic calcites
667 are subject to significant variability in solubility estimates even for specimens of similar Mg
668 content (Morse et al. 2006). Because ν_1 FWHM can quantify overall structural disorder within
669 carbonate minerals (Bischoff et al. 1985), the spectral parameter could provide a robust method
670 to incorporate non-Mg factors influencing calcite stability and therefore solubility. Increased
671 accuracy in determining biogenic calcite solubility could help determine which calcifying
672 organisms are most at risk from stressors like ocean acidification. Despite the logical connection
673 between structural disorder and mineral solubility, no experiments to date have quantified the
674 relationship between calcite solubility and ν_1 FWHM.
675
676 **Species-specific biomineralization**
677 Biomineralization patterns differ by species, especially between those residing in
678 shallower and deeper water, respectively. Certain specimens (*H. imperiale/laauense*) displayed
679 structural disorder and Mg values anticipated from a sharp radial change in skeletal growth zones
680 (i.e., from annular to medullar). However, changes in structural disorder were less striking in
681 other specimens (*P.* cf. *secundum*, *C. tortuosum*) with some patterns (*Acanella* spp.) being
682 entirely different from expectations. Such differences could be linked to vital effects involving
683 organic molecules or larger calcification mechanisms that influence the specific manner of
684 calcite precipitation and subsequent Mg incorporation. Further clarification of these species-

specific biomineralization patterns could provide insight as to how certain species precipitate skeleton differently than others as well as how such biominerals will react to future environmental change. These inter-species differences in biomineralization may also impact how useful different species are for paleo-proxy applications (reviewed in Thompson 2022).

Mg paleo-proxies

A better understanding of calcite structural disorder will clarify applications of Mg paleo-proxies. Vital effects interfere with the correlation between skeletal Mg and temperature since faster growth also enhances Mg content (Vielzeuf et al. 2018). This interference is particularly apparent in temperate waters where growth rate and temperature covary seasonally. The results from this study demonstrate the effect that growth rates on different segments of octocoral skeleton can have on Mg content despite experiencing the same environmental conditions. Correcting Mg content for vital effects will likely require the quantification and removal of growth rates with respect to changes in Mg to isolate the purely abiotic environmental effects.

Acknowledgements

Octocoral Raman analysis was supported by the Raman and Infrared Spectroscopy Laboratory at the Hawai‘i Institute for Geophysics and Planetary Sciences. We specifically thank M. Egan for micro-Raman instrument training and troubleshooting. Collection of octocoral samples and oceanographic data were made possible by the Hawai‘i Undersea Research Laboratory (HURL). Financial support for ship and submersible time were provided by the NOAA Deep Sea Coral and Sponge Research and Technology Program. We thank J. Sanchez

and L. Dueñas at the Universidad de Los Andes in Colombia and B. Lendvay at the University of Zürich for morphological and genetic identification of the octocoral specimens. Sample M3 was provided by F. Parrish from the Pacific Islands Fisheries Science Center.

References Cited

Acosta-Maeda, T.E., Scott, E.R.D., Sharma, S.K., and Misra, A.K. (2013) The pressures and temperatures of meteorite impact: Evidence from micro-Raman mapping of mineral phases in the strongly shocked Taiban ordinary chondrite. American Mineralogist, 98, 859-869.

Al-Horani, F.A., Al-Moghrabi, S.M., and de Beer, D. (2003) The mechanism of calcification and its relation to photosynthesis and respiration in the scleractinian coral Galaxea fascicularis. Marine Biology, 142, 419-426.

Andersson, A.J., Mackenzie, F.T., and Bates, N.R. (2008) Life on the margin: implications of ocean acidification on Mg-calcite, high latitude and cold-water marine calcifiers. Marine Ecology Progress Series, 373, 265-273.

Ardila NE, Giribet G, and Sánchez JA (2012) A time-calibrated molecular phylogeny of the precious corals: reconciling discrepancies in the taxonomic classification and insights into their evolutionary history. BMC Evolutionary Biology, 12, 246.

Bell, T., Nishida, K., Ishikawa, K., Suzuki, A., Nakamura, T., Sakai, K., Ohno, Y., Iguchi, A., and Yokoyama, Y. (2017) Temperature-controlled culture experiments with primary polyps of coral Acropora digitifera: Calcification rate variations and skeletal Sr/Ca, Mg/Ca, and Na/Ca ratios. Palaeogeography, Palaeoclimatology, Palaeoecology, 484, 129-

135.

Bischoff, W.D., Sharma, S.K., and Mackenzie, F.T. (1985) Carbonate ion disorder in synthetic and biogenic magnesian calcites: a Raman spectral study. American Mineralogist, 70, 581-589.

Borromeo, L., Zimmermann, U., Andò, S., Coletti, G., Bersani, D., Basso, D., Gentile, P., Schulz, B., and Garzanti, E. (2017) Raman spectroscopy as a tool for magnesium estimation in Mg-calcite. Journal of Raman Spectroscopy, 48, 983-992.

Bostock, H.C., Tracey, D.M., Currie, K.I., Dunbar, G.B., Handler, M.R., Mikaloff Fletcher, S.E., Smith, A.M., and Williams, M.J.M. (2015) The carbonate mineralogy and distribution of habitat forming deep-sea corals in the southwest Pacific region. Deep Sea Research Part I: Oceanographic Research Papers, 100, 88-104.

Calil, P.H.R., Richards, K.J., Jia, Y., and Bidigare, R.R. (2008) Eddy activity in the lee of the Hawaiian Islands. Deep Sea Research Part II: Topical Studies in Oceanography, 55, 1179-1194.

Chaabane, S., López Correa, M., Ziveri, P., Trotter, J., Kallel, N., Douville, E., McCulloch, M., Taviani, M., Linares, C., and Montagna, P. (2019) Elemental systematics of the calcitic skeleton of Corallium rubrum and implications for the Mg/Ca temperature proxy. Chemical Geology, 52, 237-258.

Chave, K.E. (1954) Aspects of biogeochemistry of magnesium 1. Calcareous marine organisms. Journal of Geology, 62, 266–283.

Comeau, S., Cornwall, C.E., DeCarlo, T.M., Krieger, E., and McCulloch, M.T. (2018) Similar controls on calcification under ocean acidification across unrelated coral reef taxa. Global Change Biology, 24, 4857-4868.

754 Cornwall, C., Comeau, S., DeCarlo, T., Moore, B., D'alexis, Q., and McCulloch, M. (2018)
755 Resistance of corals and coralline algae to ocean acidification: physiological control of
756 calcification under natural pH variability. Proceedings of the Royal Society B: Biological
757 Sciences, 285, 20181168.
758 Cornwall, C., Comeau, S., DeCarlo, T.M., Larcombe, E., Moore, B., Giltrow, K., Puerzer, F.,
759 D'Alexis, Q., and McCulloch, M.T. (2020) A coralline alga gains tolerance to ocean
760 acidification over multiple generations of exposure. Nature Climate Change, 10, 143-146.
761 Coronado, I., Fine, M., Bosellini, F.R., and Stolarski, J. (2019) Impact of ocean acidification on
762 crystallographic vital effect of the coral skeleton. Nature Communications, 10, 2896.
763 DeCarlo, T., D'Olivo, J., Foster, T., Holcomb, M., Becker, T., and McCulloch, M. (2017) Coral
764 calcifying fluid aragonite saturation states derived from Raman spectroscopy.
765 Biogeosciences, 14, 5253-5269.
766 DeCarlo, T.M., Ren, H., and Farfan, G.A. (2018) The origin and role of organic matrix in
767 coral calcification: Insights from comparing coral skeleton and abiogenic aragonite.
768 Frontiers in Marine Science, 5, 170.
769 DeCarlo, T.M., Comeau, S., Cornwall, C.E., Gajdzik, L., Guagliardo, P., Sadekov, A.,
770 Thillainath E.C., Trotter, J., and McCulloch, M.T. (2019) Investigating marine bio
771 calcification mechanisms in a changing ocean with in vivo and high-resolution ex vivo
772 Raman spectroscopy. Global Change Biology, 25, 1877-1888.
773 Dickson, A.G. (1990) Thermodynamics of the dissociation of boric acid in synthetic seawater
774 from 273.15 to 318.15 K. Deep Sea Research, 37, 755-766.
775 Dickson, A.G., and Millero, F.J. (1987) A comparison of the equilibrium constants for the
776 dissociation of carbonic acid in seawater media. Deep Sea Research, 34, 1733-1743.

777 Dickson, A.G., Sabine, C.L., and Christian, J.R. (2007) Guide to best practices for ocean CO_2
778 measurements, 191 p. PICES, Sidney.
779 Dueñas, L.F., Alderslade, P., and Sánchez, J.A. (2014) Molecular systematics of the deep-sea
780 bamboo corals (Octocorallia: Isididae: Keratoisidinae) from New Zealand with
781 descriptions of two new species of Keratoisis. Molecular Phylogenetics and Evolution,
782 74, 15-28.
783 Farfan, G.A., Cordes, E.E., Waller, R.G., DeCarlo, T.M., and Hansel, C.M. (2018) Mineralogy
784 of deep-sea coral aragonites as a function of aragonite saturation state. Frontiers in
785 Marine Science, 5, 473.
786 Farfan, G.A., Apprill, A., Cohen, A., DeCarlo, T.M., Post, J.E., Waller, R.G., and Hansel, C.M.
787 (2021) Crystallographic and chemical signatures in coral skeletal aragonite. Coral Reefs,
788 41, 19-34.
789 Farmer, J.R., Hönisch, B., Robinson, L.F., and Hill, T.M. (2015) Effects of seawater-pH and
790 biomineralization on the boron isotopic composition of deep-sea bamboo corals.
791 Geochimica et Cosmochimica Acta, 155, 86-106.
792 Flöter, S., Fietzke, J., Gutjahr, M., Farmer, J., Hönisch, B., Nehrke, G., and Eisenhauer, A.
793 (2019) The influence of skeletal micro-structures on potential proxy records in a bamboo
794 coral. Geochimica et Cosmochimica Acta, 248, 43-60.
795 Gagnon, A.C., Adkins, J.F., Fernandez, D.P., and Robinson, L.F. (2007) Sr/Ca and Mg/Ca vital
796 effects correlated with skeletal architecture in a scleractinian deep-sea coral and the role
797 of Rayleigh fractionation. Earth and Planetary Science Letters, 261, 280-295.
798 Greenwood, J. (2009) Shallow water dissolution of settling calcite at station ALOHA.
799 Limnology and Oceanography, 54, 1420-1424.

800 Hasegawa, H., Rahman, M.A., Luan, N.T., Maki, T., and Iwasaki, N. (2012). Trace elements in
801 Corallium spp. as indicators for origin and habitat. Journal of Experimental Marine
802 Biology and Ecology, 414, 1–5.
803 Hennige, S.J., Wicks, L.C., Kamenos, N.A., Perna, G., Findlay, H.S., and Roberts, J.M. (2015)
804 Hidden impacts of ocean acidification to live and dead coral framework. Proceedings of
805 the Royal Society of London B: Biological Sciences, 282, 20150990.
806 Kaabar, W., Bott, S., and Devonshire, R. (2011) Raman spectroscopic study of mixed carbonate
807 materials. Spectrochimica Acta A, 78, 136-141.
808 Kamenos, N.A., Burdett, H.L., Aloisio, E., Findlay, H.S., Martin, S., Longbone, C., Dunn, J.,
809 Widdicombe, S., and Calosi, P. (2013) Coralline algal structure is more sensitive to rate,
810 rather than the magnitude, of ocean acidification. Global Change Biology, 19, 3621-3628.
811 Kamenos, N.A., Perna, G., Gambi, M.C., Micheli, F., and Kroeker, K.J. (2016) Coralline algae
812 in a naturally acidified ecosystem persist by maintaining control of skeletal mineralogy
813 and size. Proceedings of the Royal Society of London B: Biological Sciences, 283,
814 20161159.
815 Kontoyannis, C.G., Orkoula, M.G., and Koutsoukos, P.G. (1997) Quantitative analysis of
816 sulfated calcium carbonates using Raman spectroscopy and X-ray Powder Diffraction.
817 Analyst, 122, 33-38.
818 Krishnamurti, D. (1957) The Raman spectrum of calcite and its interpretation. Proceedings of the
819 Indian Academy of Sciences, A46, 183-202.
820 LaVigne, M., Hill, T.M., Spero, H.J., and Guilderson, T.P. (2011) Bamboo coral Ba/Ca:
821 calibration of a new deep ocean refractory nutrient proxy. Earth Planetary Science
822 Letters, 312, 506-515.

823 Lebrato, M., Andersson, A.J., Ries, J.B., Aronson, R.B., Lamare, M.D., Koeve, W., Oschlies, A.,
824 Iglesias-Rodriguez, M.D., Thatje, S., Amsler, M., Vos, S.C., Jones, D.O.B., Ruhl, H.A.,
825 Gates, A.R., and McClintock, J.B. (2016) Benthic marine calcifiers coexist with $CaCO_3$-
826 undersaturated seawater worldwide. Global Biogeochemical Cycles, 30, 1038-1053.
827 Lendvay, B., Cartier, L.E., Gysi, M., Meyer, J.B., Krzemnicki, M.S., Kratzer, A., and Morf, N.V.
828 (2020) DNA fingerprinting: an effective tool for taxonomic identification of precious
829 corals in jewelry. Science Reports, 10, 1-12.
830 Lewis, E., and Wallace, D. (1998) Program developed for CO_2 system calculations: Carbon
831 Dioxide Information Analysis Center, Oak Ridge National Laboratory, ORNL/CDIAC
832 105.
833 Long, X., Ma, Y., and Qi, L. (2014) Biogenic and synthetic high magnesium calcite–A review.
834 Journal of Structural Biology, 185, 1-14.
835 Luan, N.T., Rahman, M.A., Maki, T., Iwasaki, N., and Hasegawa, H. (2013) Growth
836 characteristics and growth rate estimation of Japanese precious corals. Journal of
837 Experimental Marine Biology and Ecology, 441, 117-125.
838 Mackenzie, F.T., Bischoff, W.D., Bishop, F.C., Loijens, M., Schoonmaker, J., and Wollast, R.
839 (1983) Magnesian calcites: low temperature occurrence, solubility and solid-solution
840 behavior. In R.J. Reeder, Ed., Carbonates: Mineralogy and Chemistry, 11, p. 97-143.
841 Reviews in Mineralogy, Mineralogical Society of America, Washington, DC.
842 Mass, T., Drake, J.L., Haramaty, L., Kim, J.D., Zelzion, E., Bhattacharya, D., and Falkowski,
843 P.G. (2013) Cloning and characterization of four novel coral acid-rich proteins that
844 precipitate carbonates in vitro. Current Biology, 23, 1126-1131.
845 Mavromatis, V., Gautier, Q., Bosc, O., and Schott, J. (2013) Kinetics of Mg partition and Mg

stable isotope fractionation during its incorporation in calcite. Geochimica et Cosmochimica Acta, 114, 188-203.

McCulloch, M., Falter, J., Trotter, J., and Montagna, P. (2012) Coral resilience to ocean acidification and global warming through pH up-regulation. Nature Climate Change, 2, 623-627.

McDougall, T.J., and Barker, P.M. (2011) Getting started with TEOS-10 and the Gibbs Seawater (GSW) Oceanographic Toolbox, 28pp., SCOr/IAPSO WG127.

Mehrbach, C., Culberson, C.H., Hawley, J.E., and Pytkowicx, R.M. (1973) Measurement of the apparent dissociation constants of carbonic acid in seawater at atmospheric pressure. Limnology and Oceanography, 18, 897-907.

Merrifield, M.A., and Holloway, P.E. (2002) Model estimates of M2 internal tide energetics at the Hawaiian Ridge. Journal of Geophysical Research, 107, 3179.

Morse, J.W., Andersson, A.J., and Mackenzie, F.T. (2006) Initial responses of carbonate-rich shelf sediments to rising atmospheric pCO_2 and "ocean acidification:" role of high Mg calcites. Geochimica et Cosmochimica Acta, 70, 5814–5830.

Morse, J.W., Arvidson, R.S., and Lüttge, A. (2007) Calcium carbonate formation and dissolution. Chemical Reviews, 107, 342-381.

Mucci, A. (1987) Influence of temperature on the composition of magnesian calcite overgrowths precipitated from seawater. Geochimica et Cosmochimica Acta, 51, 1977-1984.

Murakami-Sugihara, N., Shirai, K., Hori, M., Amano, Y., Fukuda, H., Obata, H., Tanaka, K., Mizukawa, K., Sano, Y., Takada, H., and Ogawa, H. (2019) Mussel shell geochemical analyses reflect coastal environmental changes following the 2011 Tohoku tsunami. ACS Earth and Space Chemistry, 3, 1346-1352.

Pauly, M., Kamenos, N.A., Donohue, P., and LeDrew, E. (2015) Coralline algal Mg-O bond strength as a marine pCO_2 proxy. Geology, 43, 267-270.

Perrin, J., Vielzeuf, D., Ricolleau, A., Dallaporta, H., Valton, S., and Floquet, N. (2015) Block by-block and layer-by-layer growth modes in coral skeletons. American Mineralogist, 100, 681-695.

Perrin, J., Vielzeuf, D., Laporte, D., Ricolleau, A., Rossman, G.R., and Floquet, N. (2016) Raman characterization of synthetic magnesian calcites. American Mineralogist, 101, 2525-2538.

R Core Team (2021) R: A language and environment for statistical computing. Vienna, Austria: R Foundation for Statistical Computing.

Riebesell, U., Fabry, V.J., Hansson, L., and Gattuso, J.P. (2010). Guide to best practices for ocean acidification research and data reporting, 260 p., Publications Office of the European Union, Luxembourg.

Robinson, L.F., Adkins, J.F., Frank, N., Gagnon, A.C., Prouty, N.G., Roark, E.B., and van de Flierdt, T. (2014) The geochemistry of deep-sea coral skeletons: a review of vital effects and applications for paleoceanography. Deep Sea Research Part II: Topical Studies in Oceanography, 99, 184-198.

Rollion-Bard, C., and Blamart, D. (2015) Possible controls on Li, Na, and Mg incorporation into aragonite coral skeletons. Chemical Geology, 396, 98-111.

Sherwood, O.A., Heikoop, J.M., Sinclair, D.J., Scott, D.B., Risk, M.J., Shearer, C., and Azetsu Scott, K. (2005) Skeletal Mg/Ca in Primnoa resedaeformis: relationship to temperature. In A. Freiwald and J.M. Roberts, Eds., Cold-water Corals and Ecosystems, p. 1061-1079, Springer-Verlag, Berlin.

892 Shibano, Y., Takahata, K., Kawano, J., Watanabe, T., Enomoto, D., Kagi, H., Kamiya, N., and
893 Yamamoto, J. (2017) Raman spectroscopic determination of Sr/Ca ratios of calcite
894 samples. Journal of Raman Spectroscopy, 48, 1755-1761.
895 Sinclair, D.J., Williams, B., Allard, G., Ghaleb, B., Fallon, S., Ross, S.W., and Risk, M. (2011)
896 Reproducibility of trace element profiles in a specimen of the deep-water bamboo coral
897 Keratoisis sp. Geochimica et Cosmochimica Acta, 75, 5101-5121.
898 Tambutté, S., Holcomb, M., Ferrier-Pagés, C., Reynaud, S., Tambutté, E., Zoccola, D., and
899 Allemand, D. (2011) Coral biomineralization: from gene to the environment. Journal of
900 Experimental Marine Biology and Ecology, 408, 58-78.
901 Thompson, D.M. (2022) Environmental records from coral skeletons: A decade of novel insights
902 and innovation. Wiley Interdisciplinary Reviews: Climate Change, 13, e745.
903 Thresher, R., Rintoul, S.R., Koslow, J.A., Weidman, C., Adkins, J., and Proctor, C. (2004)
904 Oceanic evidence of climate change in southern Australia over the last three centuries.
905 Geophysical Research Letters, 31, L07212.
906 Thresher, R.E., MacRae, C.M., Wilson, N.C., and Gurney, R. (2007) Environmental effects on
907 the skeletal composition of deep-water gorgonians (Keratoisis spp.; Isididae). Bulletin of
908 Marine Science, 81, 409-422.
909 Thresher, R.E., Wilson, N.C., MacRae, C.M., and Neil, H. (2010) Temperature effects on the
910 calcite skeletal composition of deep-water gorgonians (Isididae). Geochimica et
911 Cosmochimica Acta, 74, 4655-4670.
912 Thresher, R.E., Tilbrook, B., Fallon, S., Wilson, N.C., and Adkins, J. (2011) Effects of chronic

low carbonate saturation levels on the distribution, growth and skeletal chemistry of deep-sea corals and other seamount megabenthos. Marine Ecology Progress Series, 442, 87-99.

Thresher, R.E., Fallon, S.J., and Townsend, A.T. (2016) A "core-top" screen for trace element proxies of environmental conditions and growth rates in the calcite skeletons of bamboo corals (Isididae). Geochimica et Cosmochimica Acta, 193, 75-99.

Uppström, L.R. (1974) The boron/chlorinity ratio of deep-sea water from the Pacific Ocean. Deep Sea Research and Oceanographic Abstracts, 21, 161-162.

Urmos, J., Sharma, S.K., and Mackenzie, F.T. (1991) Characterization of some biogenic carbonates with Raman spectroscopy. American Mineralogist, 76, 641-646.

Vielzeuf, D., Garrabou, J., Baronnet, A., Grauby, O., and Marschal, C. (2008) Nano to macroscale biomineral architecture of red coral (Corallium rubrum). American Mineralogist, 93, 1799-1815.

Vielzeuf, D., Garrabou, J., Gagnon, A., Ricolleau, A., Adkins, J., Günther, D., Hametner, K., Devidal, J-L., Reusser, E., and Perrin, J. (2013) Distribution of sulphur and magnesium in the red coral. Chemical Geology, 355, 13-27.

Vielzeuf, D., Gagnon, A.C., Ricolleau, A., Devidal, J-L., Balme-Heuze, C., Yahiaoui, N., Fonquernie, C., Perrin, J., Garrabou, J., and Montel, J-M. (2018) Growth kinetics and distribution of trace elements in precious corals. Frontiers in Earth Science, 6, 167.

Wang, D., Hamm, L.M., Bodnar, R.J., and Dove, P.M. (2012) Raman spectroscopic characterization of the magnesium content in amorphous calcium carbonates. Journal of Raman Spectroscopy, 43, 543-548.

Watson, E.B. (2004) A conceptual model for near-surface kinetic controls on the trace-element

and stable isotope composition of abiogenic calcite crystals. Geochimica et Cosmochimica Acta, 68, 1473-1488.

Weinbauer, M., Brandstätter, F., and Velimirov, B. (2000) On the potential use of magnesium and strontium concentrations as ecological indicators in the calcite skeleton of the red coral (Corallium rubrum). Marine Biology, 137, 801-809.

White, W. (1974) The carbonate minerals. In E.V.C. Farmer, Ed., The Infrared Spectra of Minerals, Mineralogical Society Monograph, 4, p. 87-110, Mineralogical Society, London.

Yoshimura, T., Tanimizu, M., Inoue, M., Suzuki, A., Iwasaki, N., and Kawahata, H. (2011) Mg isotope fractionation in biogenic carbonates of deep-sea coral, benthic foraminifera, and hermatypic coral. Analytical and Bioanalytical Chemistry, 401, 2755-2769.

Figure Captions

Figure 1. Octocoral and oceanographic sampling sites including the Makapu‘u site for sample M3.

Figure 2. Spatially mapped relative Mg content (color-coded, count/count) of a Corallidae octocoral cross section taken using Electron Microprobe Analysis (EMPA, see Supplementary[1] Info., Figures, and Tables) and a corresponding photograph of the sample. The central medullar region of skeleton contains elevated Mg content and is surrounded by annular skeleton

(annotated in the EMPA image). Up current and down current sides of axial skeleton are annotated in the photograph.

Figure 3. (a) Relationship between Mg content calculated from ν_1 Raman shift (Perrin et al. 2016) and Mg measured using LA-ICPMS (N = 90). The 1:1 line is shown in black. **(b)** Radial measurements of octocoral Mg content from *P.* cf. *secundum* 238 m (slow-axis) taken using the Raman ν_1 peak (black, N = 26) and LA-ICPMS (blue, N = 26) **(c)** as well as the relationship between the two. All error bars represent ±1 SD with the shaded regions representing the 95% CI. Note that the data from subplot **(b)** was taken along a radial transect from the cross section surface to the inner medullar region (see Fig. 2 for a visual example).

Figure 4. Mean ν_1 FWHM, Mg content (from ν_1 Raman shift), and residual ν_1 FWHM of octocoral surface skeleton (N = 28) with respect to potential density (an analog of depth). Error bars represent ±1 SD and the shaded regions represent the 95% CI.

Figure 5. Mean ν_1 FWHM of octocoral surface skeleton with respect to major oceanographic variables covered in this study (N = 28). Error bars represent ±1 SD and the shaded regions represent the 95% CI.

Figure 6. Mean Mg content (from ν_1 Raman shift) of octocoral surface skeleton with respect to major oceanographic variables covered in this study (N = 28). Error bars represent ±1 SD and the shaded regions represent the 95% CI.

Figure 7. Mean intra-sample octocoral ν_1 FWHM, Mg content (from ν_1 Raman shift, abbreviated as "RS"), and residual ν_1 FWHM with respect to octocoral branch diameter for three of the five specific samples (each with N = 100) **(a)** *P.* cf. *secundum* from 273 m; **(b)** *H. imperiale/laauense* from 444 m; **(c)** *Acanella* spp. from 823 m. All specimens are shown in [1]Fig. S7. Each measurement location (a five-point transect) is shown by the red markers. Branch diameter serves as a proxy for ontogenetic growth rates (e.g., smaller branches = faster skeletal growth). A general additive model was used for the trendlines where error bars are ±1 SD, shaded regions are the 95% CI, and DevExpl represents the deviance explained by the model.

Figure 8. (a) Mean ν_1 FWHM compared to mean Mg-based ν_1 FWHM, **(b)** mean ν_1 FWHM compared to mean residual ν_1 FWHM, and **(c)** mean Mg content (from ν_1 Raman shift) compared to mean residual ν_1 FWHM for the five octocoral specimens used during the intra-sample variability measurements (N = 100 for each specimen). Error bars are ±1 SD while shaded regions are the 95% CI.

Figure 9: Mg-temperature relationships from this study and other relevant octocoral or inorganic calcite studies (authors annotated). Data from this study are shown with triangle markers. Shaded regions represent the 95% CI around the trendlines. The red dashed line represents the relationship from Mucci (1987). N-values and trendline statistics are displayed in [1]Table S6.
A: Chave 1954; Weinbauer et al. 2000; Yoshimura et al. 2011; Thresher et al. 2016
B: Yoshimura et al. 2011; Vielzeuf et al. 2013; Chaabane et al. 2019

Deposit Items

[1]Deposit Item, Supplementary Info.

Oceanographic data adjustments using seawater potential density

Oceanographic data were adjusted as the CTD casts and discrete bottle samples only provide a depth-based snapshot of mid-water environmental conditions. While sessile benthic organisms like octocorals are fixed at depth, oceanographic parameters are tightly fixed to density-specific water masses, which can undergo constant vertical oscillations from physical forcing, thereby exposing octocorals to a range of environmental conditions over short timescales. Inertial oscillations in seawater masses are apparent through high-resolution temperature data collected from Kailua-Kona, which can be driven by factors such as lunar tides and larger mesoscale eddies. Such oscillations also visibly attenuate with increasing depth and can influence oceanographic measurements conducted at a fixed depth depending on the time of sampling. The temperature time-series data, as well as correlations between temperature and potential density (σ_θ, kg/m^3) from the CTD casts, provided insight on the magnitude of water mass oscillations over different depths and times and allowed for CTD measurement adjustments. A temperature and σ_θ correlation converted high-resolution temperature data over multiple depths into high-resolution σ_θ data which was then averaged by depth over a 24-hour composite period (e.g., changes in σ_θ relative to mean σ_θ ($\Delta\sigma_\theta$) as a function of time of day). The depth and timing of specific oceanographic measurements were inserted into the 24-hour averaged curves to calculate $\Delta\sigma_\theta$. A more accurate σ_θ ($\sigma_{\theta,True}$) was then calculated through

$$\sigma_{\theta,True} = \sigma_{\theta,Measured} + \Delta\sigma_\theta \quad \text{(S1)}$$

which approximated a more accurate corresponding oceanographic parameter depending on the relationship between said parameter and $\sigma_{\theta,True}$.

Temperature data from multiple depths ranging from 220 to 900 m depict short-term (M_2 semidiurnal tidal cycles; Merrifield and Holloway 2002) and long-term (mesoscale eddies; Calil et al. 2008) variability resulting from the oscillations of water masses with different densities over a yearlong interval ([1]Fig. S2). Deviations from the average potential density were relatively small (~0.01 kg/m^3 at most) and resulted in few adjustments in depth-based oceanographic data ([1]Fig. S5). Power spectral density analysis revealed consistent tidal patterns dominated by the M_2 semidiurnal tide, which decreased rapidly with increasing depth ([1]Fig. S6). Average temperatures decreased rapidly after the 220 m logger (average temperature of 16.29 ± 1.32 °C compared to 11.02 ± 0.79 °C from 302 m) but then stabilized at 506 m and greater (6.80 ± 0.29 °C).

LA-ICPMS Reference Materials

For LA-ICPMS measurements, the reference material NIST SRM 612 was used as an external standard, with the reference materials coral powder JCp-1 and giant clam powder JCt-1 (National Institute of Advanced Industrial Science and Technology, Tsukuba, Japan) measured to confirm accuracy. The reference materials were analyzed three times before and after every 50–100 sample spots to monitor instrument drift. The Mg/Ca ratio calculations were based on the analyses of NIST SRM 612, standard glass, and reproducibility (percent relative standard deviation [%RSD]), measured at <5%. The Mg/Ca ratio of JCp-1 (certified value of Mg/Ca = 4.2 mmol/mol) was determined to be Mg/Ca = 4.5 ± 0.2 (1σ, N = 26) mmol/mol. Detailed analytical conditions are reported in the literature (e.g., Murakami-Sugihara et al. 2019).

Raman measurements of octocoral Mg and FWHM using the ν_1 peak

1049 The ν_1 peak is the strongest in the Mg-calcite spectrum and has been measured in
1050 numerous studies of biogenic aragonite (Kamenos et al. 2013, 2016; Hennige et al. 2015; Pauly
1051 et al. 2015; DeCarlo et al. 2017, 2018, 2019; Comeau et al. 2018; Cornwall et al. 2018, 2020;
1052 Farfan et al. 2018, 2021) and Mg-calcite (Bischoff et al. 1985; Urmos et al. 1991; Borromeo et
1053 al. 2017; Comeau et al. 2018; Cornwall et al. 2018, 2020). ν_1 has also been measured for
1054 amorphous calcium carbonate (Wang et al. 2012) and was noted by Borromeo et al. (2017) to be
1055 the most reliable peak (along with ν_4) for distinguishing Mg content in biogenic calcites. While
1056 the ν_1 peak is a non-degenerate (singlet) peak corresponding to the symmetric stretching
1057 vibrational mode of oxygen with respect to the carbon atom, high Mg content (~30 mol%) is
1058 known to cause asymmetry in the ν_1 peak leading to the fitting of two peaks (Perrin et al. 2016
1059 supplementary materials). However, the octocoral Mg content measured in this study does not
1060 exceed 14.5 mol%, meaning that the ν_1 peak doubling phenomenon and resulting inaccuracies in
1061 fitting Raman shift and FWHM parameters should be minimal.
1062 The intensities of the Raman spectral lines are sensitive to crystallite orientation within
1063 the analyzed sample. However, the positions (Raman shift) and line widths (FWHM) are
1064 independent of crystallite orientation. Because of this reason, Raman spectroscopy is considered
1065 a suitable technique for analyzing octocoral samples without polishing the surface skeleton.
1066 Polishing the surface skeleton would require removing sample material which would disrupt the
1067 connection between skeletal geochemistry and environmental to be measured at the time of
1068 octocoral sample collection.
1069 The Mg content of the octocoral surface skeleton was calculated using the ν_1 peak
1070 calibration lines from Perrin et al. (2016). The calibration line for ν_1 Raman shift was
1071 $$\text{Raman shift } (cm^{-1}) = 0.256 \times [MgCO_3 \text{ (mol\%)}] + 1085.71 \ (R^2 = 0.988, N = 20) \quad \text{(S2)}$$

This is the peer-reviewed, final accepted version for American Mineralogist, published by the Mineralogical Society of America.
The published version is subject to change. Cite as Authors (Year) Title. American Mineralogist, in press.
DOI: https://doi.org/10.2138/am-2022-8406. http://www.minsocam.org/

1072 which covers a range of 0 to 50 mol% $MgCO_3$. Overall ν_1 FWHM can be partitioned into a Mg-
1073 driven component (Mg-driven ν_1 FWHM) and a non-Mg component (residual ν_1 FWHM). Mg-
1074 driven ν_1 FWHM is calculated by applying the Mg content from the ν_1 Raman shift calibration
1075 line to the ν_1 FWHM calibration line:
1076 $\text{FWHM } (cm^{-1}) = -0.00787 \times [MgCO_3 \text{ (mol\%)}]^2 + 0.51 \times [MgCO_3 \text{ (mol\%)}] + 3.61$
1077 ($R^2 = 0.973$, N = 15) (S3)
1078 Residual ν_1 FWHM is the difference between the overall ν_1 FWHM signal and Mg-driven ν_1
1079 FWHM.
1080 Since concentrations and variability of Mg in octocoral skeleton are notably greater than
1081 that of other seawater ions (e.g., Sr, Ba, B), observed changes in ν_1 Raman shift should be
1082 predominantly driven by incorporated Mg. For instance, octocoral Sr/Ca and B/Ca had ranges of
1083 only around 1.26 mmol/mol and 59 μmol/mol, respectively (Farmer et al. 2015; Vielzeuf et al.
1084 2018). Using the ratios from Farfan et al. (2021), this translates to Raman shift decreases of
1085 0.069 cm^{-1} and 0.023 cm^{-1}, which are small compared to the expected 1.67 cm^{-1} increase from
1086 Mg based on Mg/Ca ranges (~64 mmol/mol) from Vielzeuf et al. (2018). A similar outcome is
1087 reached with respect to FWHM for those ranges in Mg/Ca (+1.91 cm^{-1}), Sr/Ca (-0.047 cm^{-1}), and
1088 B/Ca (-0.018 cm^{-1}). Farfan et al. 2021 did not measure Ba/Ca, but its concentration in octocorals
1089 (range of 8.1 μmol/mol) is less than that of B/Ca (Vielzeuf et al. 2018).
1090
1091 **EMPA measurement of octocoral cross section**
1092 High-resolution spatial patterns in Mg were measured within single cross section sample
1093 of Corallidae (species unknown, Taiwan). The octocoral cross section was first polished and
1094 coated with Pt-Pd before analysis. The two-dimensional distribution of Mg and Ca of the cross

section was observed using an electron microprobe analyzer (JXA-8900, JOEL) at the Atmosphere and Ocean Research Institute, The University of Tokyo. The analysis was carried out with the following settings: 15 kV accelerating voltage; 200 nA probe current; 150 sec dwell time; and 10 μm probe diameter. The distribution of Mg/Ca count ratios was visualized using ImageJ software (NIH, USA).

Tables

Table 1: Metadata for all depth gradient octocoral samples and M3 from Makapu‘u.

Sample ID#	Date/Time Sampled	Depth (m)	Location	Species	LA-ICPMS?
108	9/5/2016, 3:34pm	221	Kailua-Kona	*Pleurocorallium* cf. *secundum*	Yes
107	9/5/2016, 2:29pm	238	Kailua-Kona	*Pleurocorallium* cf. *secundum*	Yes
204	9/5/2016, 3:12pm	269	Kailua-Kona	*Pleurocorallium* cf. *secundum*	No
106	9/5/2016, 2:06pm	273	Kailua-Kona	*Pleurocorallium* cf. *secundum*	No
1105	9/28/2011, 12:33pm	280	Kealakekua	*Corallium tortuosum*	No
105	9/5/2016, 1:40pm	293	Kailua-Kona	*Corallium tortuosum*	No
1124	9/30/2011, 2:00pm	395	Wai‘ahukini	*Hemicorallium imperiale/laauense*	Yes
1126	9/30/2011, 2:44pm	396	Wai‘ahukini	*Acanella* spp.	No
1101	9/28/2011, 1:45pm	399	Kealakekua	*Hemicorallium imperiale/laauense*	Yes
1112	9/29/2011, 11:28am	401	Ho‘okena	*Hemicorallium imperiale/laauense*	No
1114	9/29/2011, 12:22pm	402	Ho‘okena	*Hemicorallium imperiale/laauense*	No
104	9/5/2016, 1:16pm	405	Kailua-Kona	*Acanella* spp.	No
1121	9/30/2011, 9:44am	444	Wai‘ahukini	*Hemicorallium imperiale/laauense*	No
1120	9/30/2011, 8:56am	445	Wai‘ahukini	*Hemicorallium imperiale/laauense*	No
1104	9/28/2011, 10:00am	446	Kealakekua	*Hemicorallium imperiale/laauense*	No
314	8/30/2017	447	1919 Lava Flow*	*Hemicorallium imperiale/laauense*	No
1109	9/29/2011, 9:18am	449	Ho‘okena	*Hemicorallium imperiale/laauense*	No
1110	9/29/2011, 10:01am	449	Ho‘okena	*Hemicorallium imperiale/laauense*	No
1117	9/29/2011, 3:29pm	449	Ho‘okena	*Hemicorallium imperiale/laauense*	No
1103	9/28/2011, 9:47am	451	Kealakekua	*Acanella* spp.	No
103	9/5/2016, 12:30pm	472	Kailua-Kona	*Hemicorallium imperiale/laauense*	No
202	9/5/2016, 1:49pm	506	Kailua-Kona	*Hemicorallium imperiale/laauense*	No
304	8/29/2017, 12:57pm	544	Kailua-Kona	*Hemicorallium imperiale/laauense*	No
313	8/30/2017	560	1919 Lava Flow*	*Hemicorallium imperiale/laauense*	Yes
312	8/30/2017	574	1919 Lava Flow*	*Hemicorallium imperiale/laauense*	Yes
102	9/5/2016, 11:45am	582	Kailua-Kona	*Hemicorallium imperiale/laauense*	Yes
303	8/29/2017, 11:27am	753	Kailua-Kona	*Acanella* spp.	No
101	9/5/2016, 10:56am	823	Kailua-Kona	*Acanella* spp.	No
M3	2/5/2000	417	Makapu‘u	*Hemicorallium imperiale/laauense*	Yes

Note: The 1919 Lava Flow site was just south of the Ho‘okena site.

This is the peer-reviewed, final accepted version for American Mineralogist, published by the Mineralogical Society of America.
The published version is subject to change. Cite as Authors (Year) Title. American Mineralogist, in press.
DOI: https://doi.org/10.2138/am-2022-8406. http://www.minsocam.org/

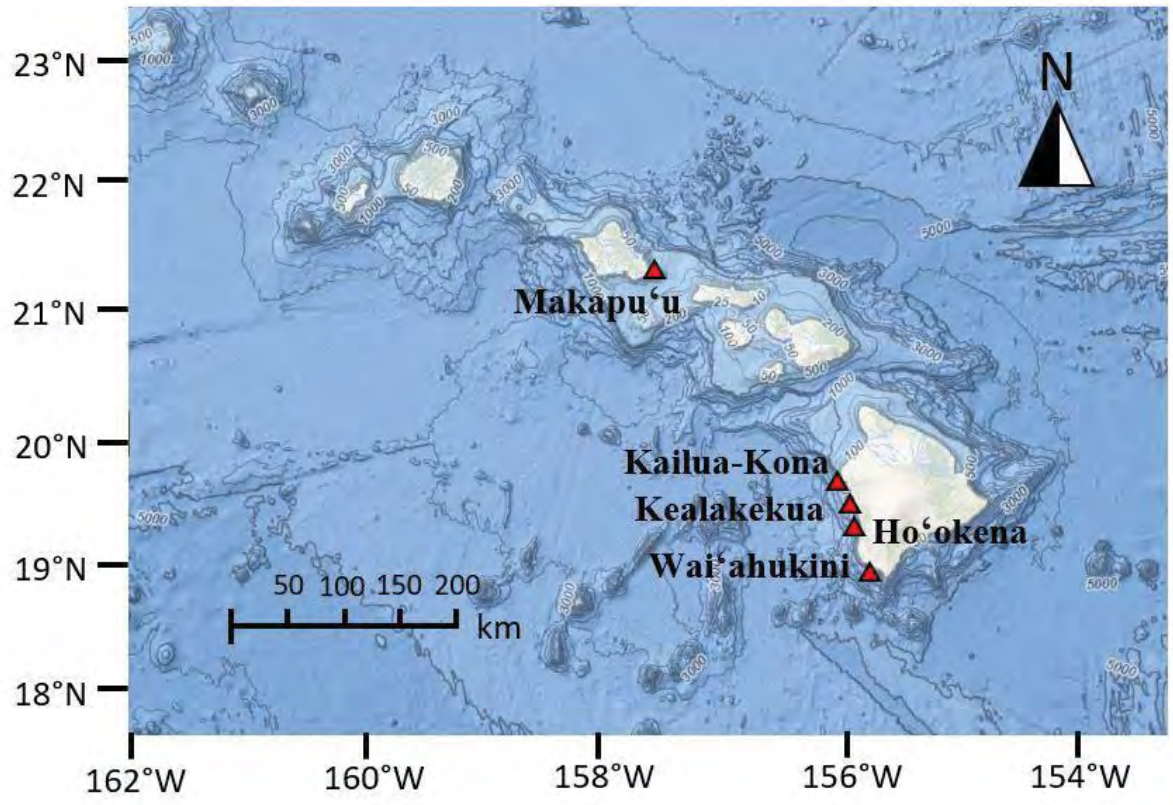

Figure 1

This is the peer-reviewed, final accepted version for American Mineralogist, published by the Mineralogical Society of America.
The published version is subject to change. Cite as Authors (Year) Title. American Mineralogist, in press.
DOI: https://doi.org/10.2138/am-2022-8406. http://www.minsocam.org/

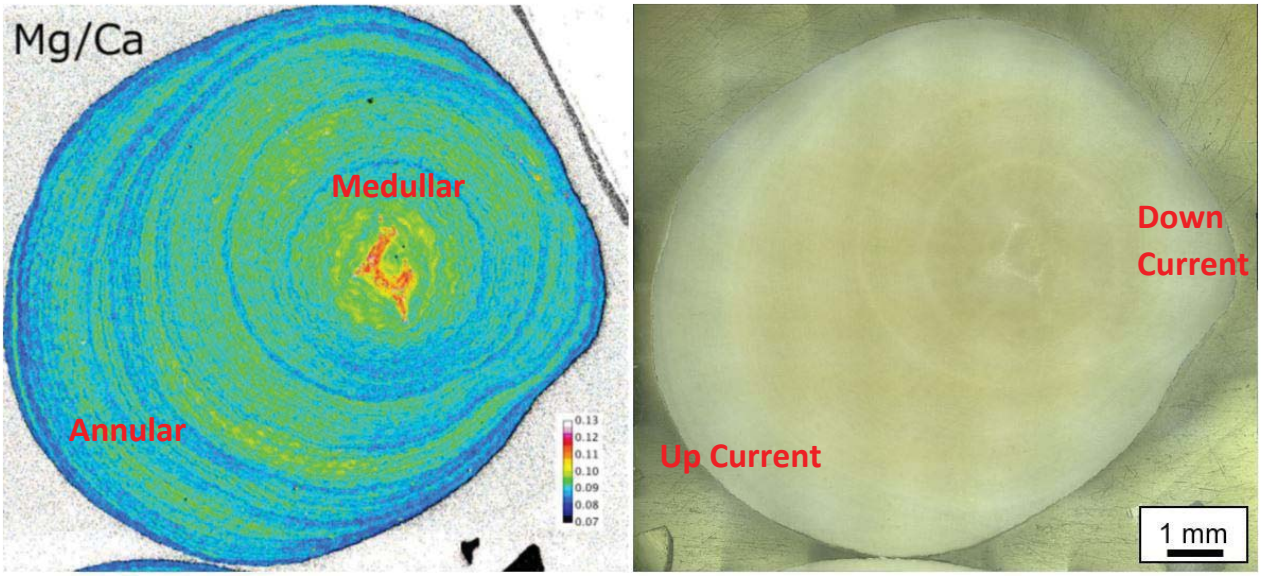

Figure 2

This is the peer-reviewed, final accepted version for American Mineralogist, published by the Mineralogical Society of America.
The published version is subject to change. Cite as Authors (Year) Title. American Mineralogist, in press.
DOI: https://doi.org/10.2138/am-2022-8406. http://www.minsocam.org/

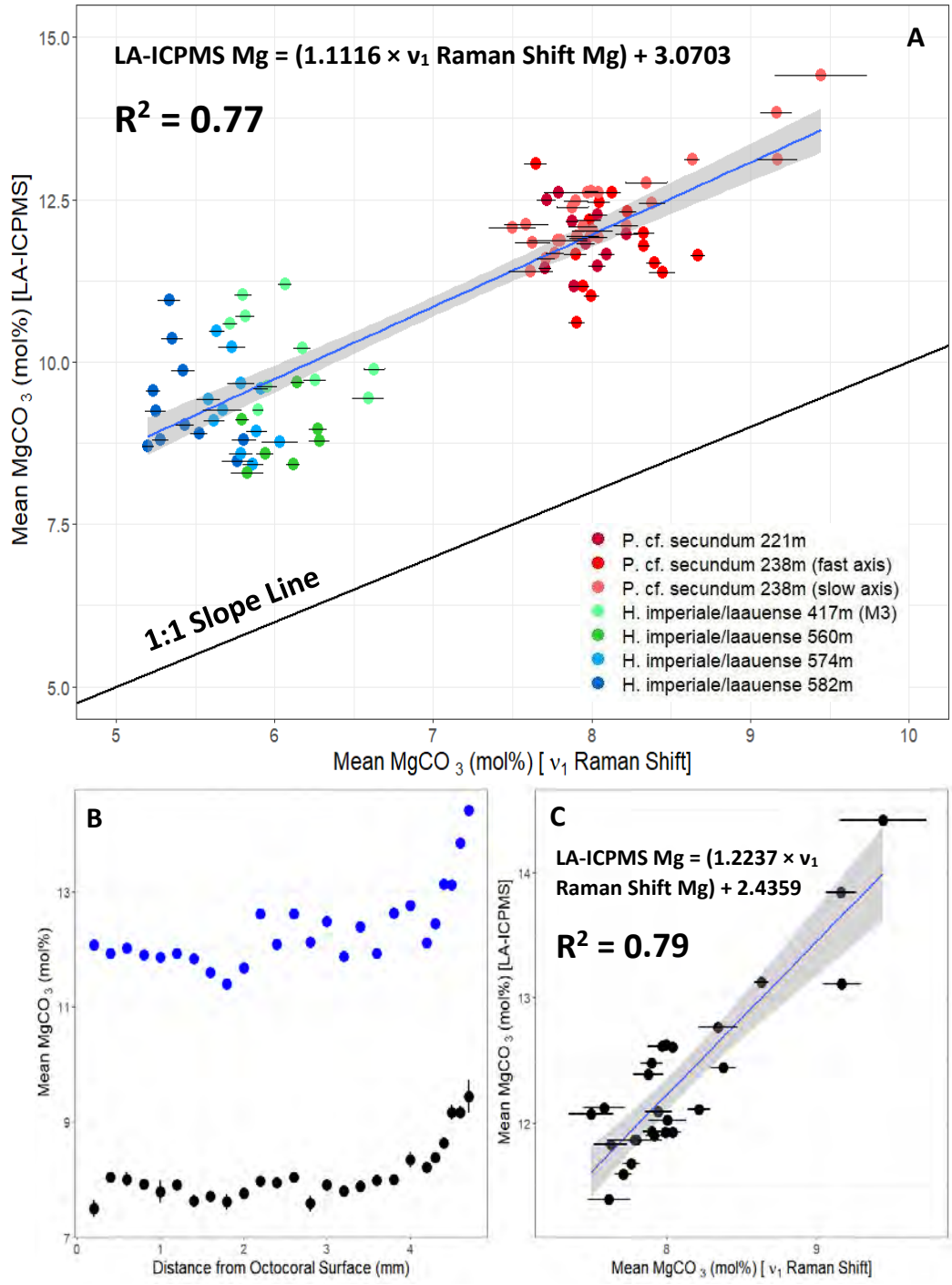

Figure 3

This is the peer-reviewed, final accepted version for American Mineralogist, published by the Mineralogical Society of America.
The published version is subject to change. Cite as Authors (Year) Title. American Mineralogist, in press.
DOI: https://doi.org/10.2138/am-2022-8406. http://www.minsocam.org/

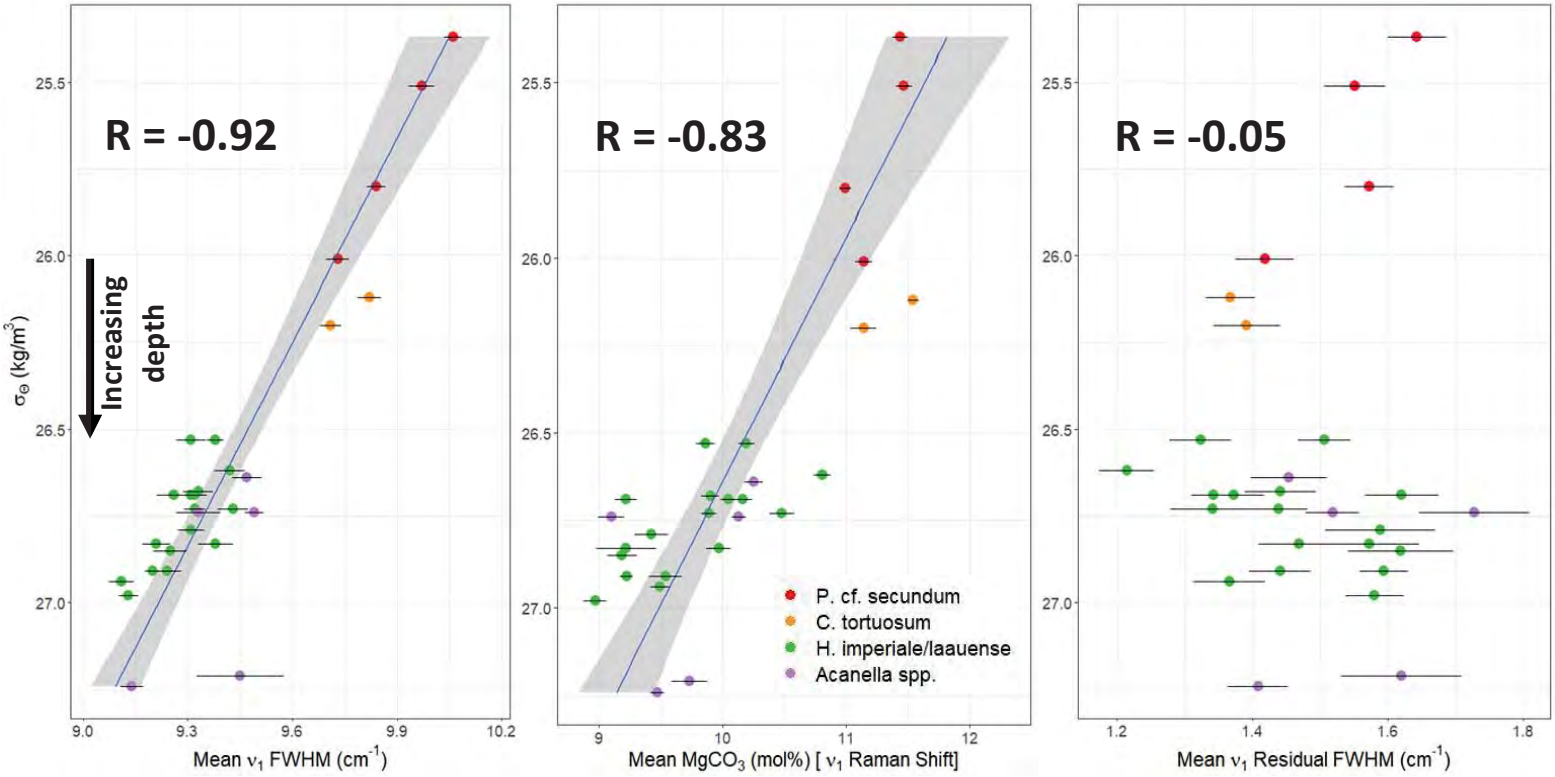

Figure 4

This is the peer-reviewed, final accepted version for American Mineralogist, published by the Mineralogical Society of America.
The published version is subject to change. Cite as Authors (Year) Title. American Mineralogist, in press.
DOI: https://doi.org/10.2138/am-2022-8406. http://www.minsocam.org/

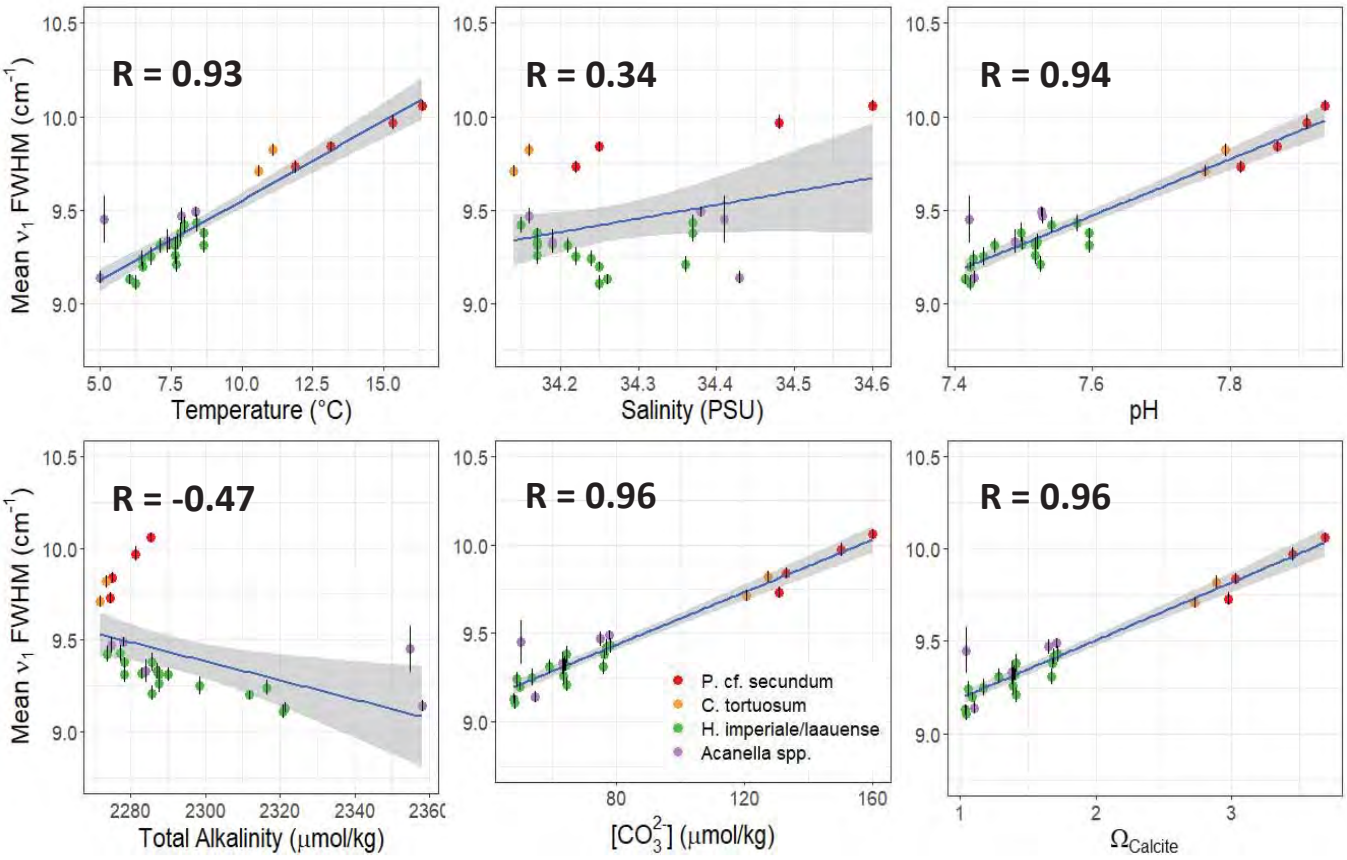

Figure 5

This is the peer-reviewed, final accepted version for American Mineralogist, published by the Mineralogical Society of America.
The published version is subject to change. Cite as Authors (Year) Title. American Mineralogist, in press.
DOI: https://doi.org/10.2138/am-2022-8406. http://www.minsocam.org/

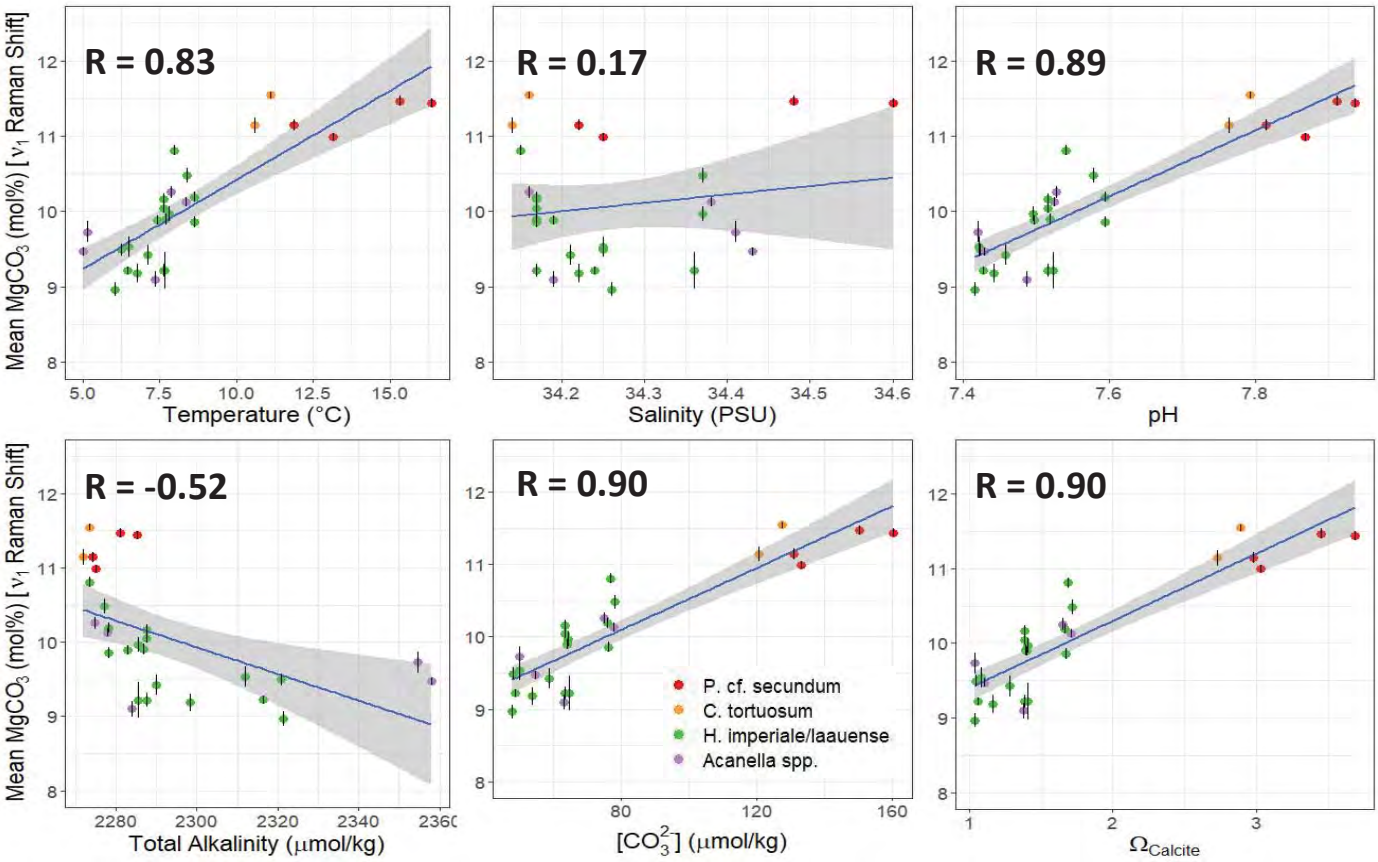

Figure 6

This is the peer-reviewed, final accepted version for American Mineralogist, published by the Mineralogical Society of America.
The published version is subject to change. Cite as Authors (Year) Title. American Mineralogist, in press.
DOI: https://doi.org/10.2138/am-2022-8406. http://www.minsocam.org/

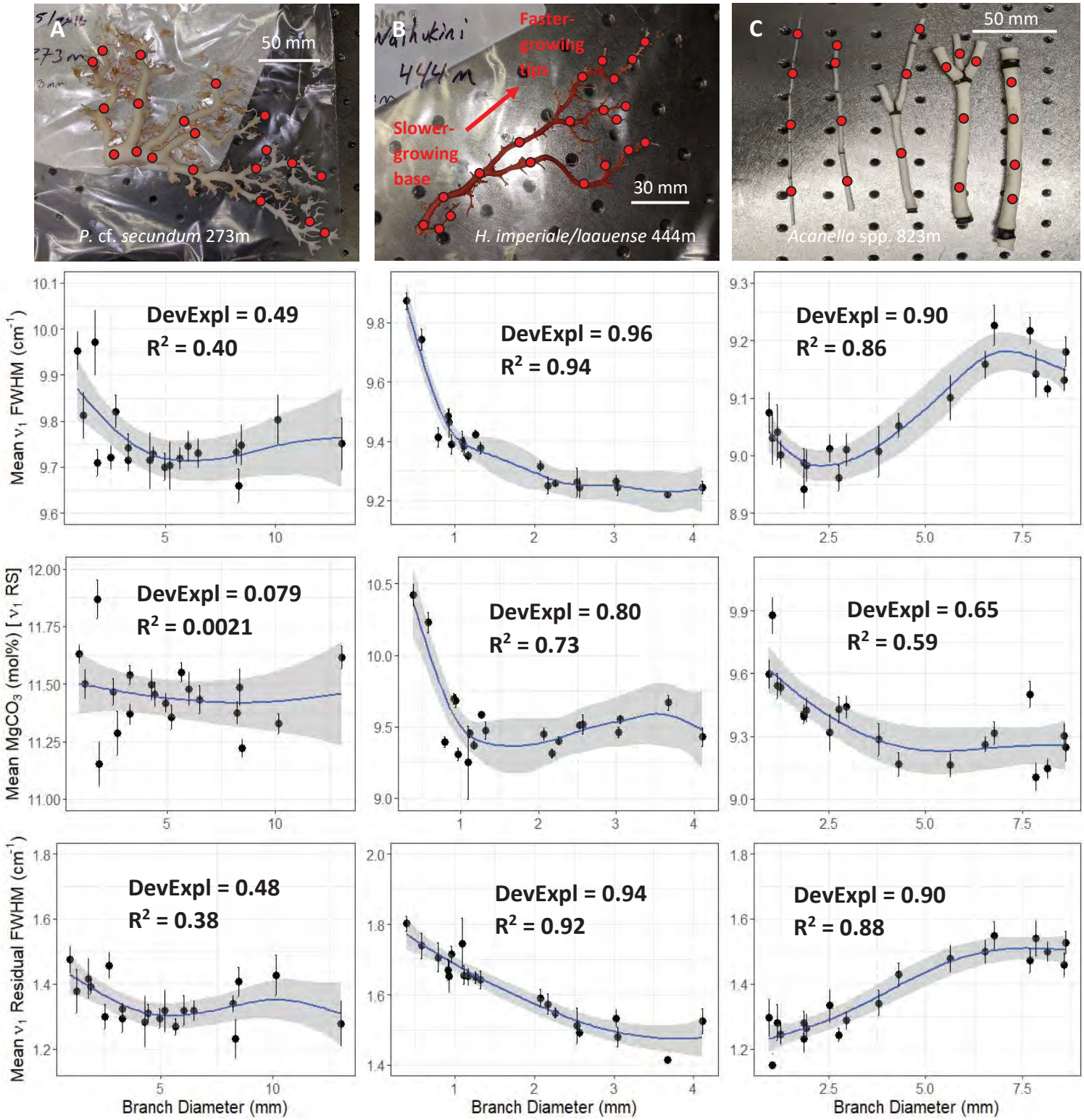

Figure 7

This is the peer-reviewed, final accepted version for American Mineralogist, published by the Mineralogical Society of America.
The published version is subject to change. Cite as Authors (Year) Title. American Mineralogist, in press.
DOI: https://doi.org/10.2138/am-2022-8406. http://www.minsocam.org/

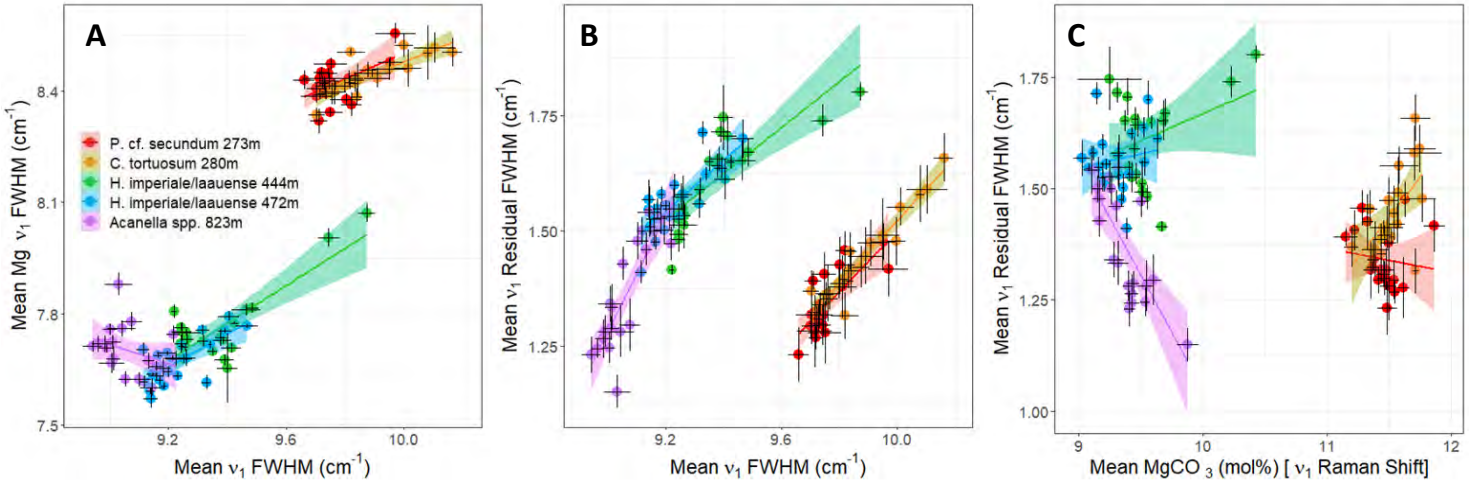

Figure 8

This is the peer-reviewed, final accepted version for American Mineralogist, published by the Mineralogical Society of America.
The published version is subject to change. Cite as Authors (Year) Title. American Mineralogist, in press.
DOI: https://doi.org/10.2138/am-2022-8406. http://www.minsocam.org/

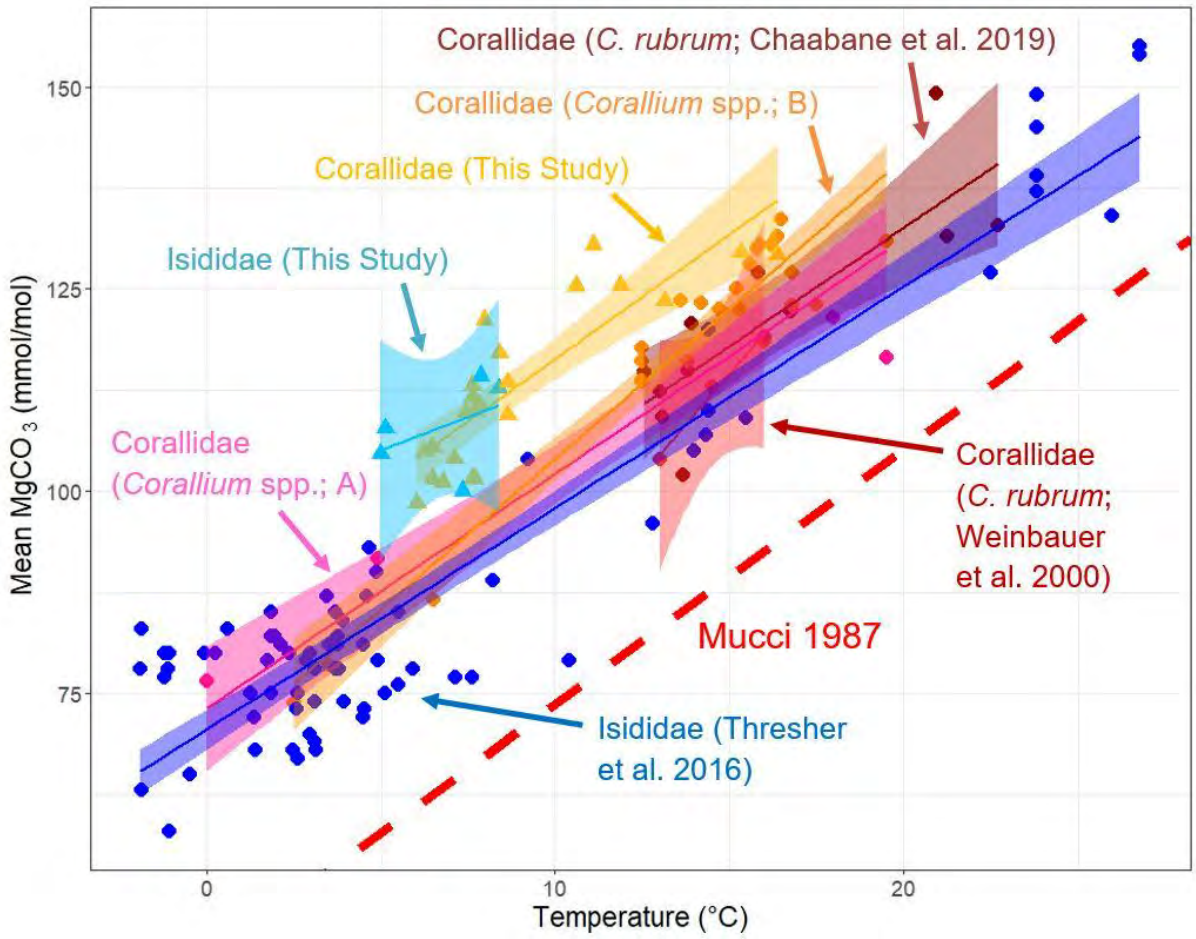

Figure 9